

**Inhomogeneity Correction in High Field  
Magnetic Resonance Images:  
Human Brain Imaging at 7 Tesla**

Elda Fischi Gómez

Assistants :Dr. Meritxell Bach Cuadra, Xavier Peña Piña  
Director: Prof. Dr. Jean-Philippe Thiran

Signal Processing Institute (ITS),  
Swiss Federal Institute of Technology (EPFL)

Universitat Politècnica de Catalunya (UPC)

July 2008

# Abstract

Magnetic Resonance Imaging, MRI, is one of the most powerful and harmless ways to study human inner tissues. It gives the chance of having an accurate insight into the physiological condition of the human body, and specially, the brain. Following this aim, in the last decade MRI has moved to ever higher magnetic field strength that allow us to get advantage of a better signal-to-noise ratio. This improvement of the SNR, which increases almost linearly with the field strength, has several advantages: higher spatial resolution and/or faster imaging, greater spectral dispersion, as well as an enhanced sensitivity to magnetic susceptibility. However, at high magnetic resonance imaging, the interactions between the RF pulse and the high permittivity samples, which causes the so called *Intensity Inhomogeneity* or  $B_1$  inhomogeneity, can no longer be negligible. This inhomogeneity causes undesired effects that affects quantitatively image analysis and avoid the application classical intensity-based segmentation and other medical functions. In this Master thesis, a new method for Intensity Inhomogeneity correction at high field is presented. At high field is not possible to achieve the estimation and the correction directly from the corrupted data. Thus, this method attempt the correction by acquiring extra information during the image process, the RF map. The method estimates the inhomogeneity by the comparison of both acquisitions. The results are compared to other methods, the PABIC and the Low-Pass Filter which try to correct the inhomogeneity directly from the corrupted data.

# Acknowledgements

This work was carried out between October 2007 and July 2008 at the Signal Processing Institute of the Swiss Federal Institute of Technology site in Lausanne, Switzerland, in collaboration with the Siemens Research Group at the CIBM/LIFMET.

This nearly a year of work, makes me owe thanks to much people. First, of course, I would like to thank the director of my Master Thesis, Professor Jean-Philippe Thiran for giving me the possibility of working at the LTS, and for making me feel part of one of the best Groups of Research I would ever met. Thanks for his advices, and specially for encouraging me to keep on even the results were not as good as I expected. Thanks for "that's research, don't worry!" ...and for showing me the way it was. I would also want to thanks Dr. Meritxell Bach Quadra and Xavier Peña Piña, my supervisors, for being always there and for answering every single question without loosing the smile (even if they were overload by their own work). Thanks for always find a piece of time for me. And, obviously, thanks to Gunnar Krueger and Jose Marques, and all the Siemens Research Group at the CIBM for their collaboration and availability during these months. And to all the people at the LTS, lab-mates and staff for make thinks easier.

It would be not fair if I don't thank the almost main responsible of my travel. Thanks Ferran Marques for giving me the last push to come here and for having been there, at the UPC, during my years of degree (not few, actually). Even in the bad moments, when the pressure almost bring me to drop out, it was really good to have someone who understood your situation. To feel you're not a number but a person, and that sometimes, is not bad to fail. Thanks to Gregorio Vazquez too, for telling me is not the time you take to do it but how you do it, that makes the difference.

My warmest thanks to my parents. Mum and Dad, this is because of you. Thanks for everything, for living and for being there always, in every case and without conditions. Thanks for show me how to be a good person, how to be honest, to try to act with modesty and to fight for my dreams. There are no words...nothing that I can say at this point could show exactly how much have you both done for me. I love you so much.

Erika (nina, ya sabes). My sister, my love, my complement. No words. Useless. Thanks, thanks for being you and me at the same time. Thanks for tell me, when I was in the train coming here, "just enjoy, no panic...just live". Thanks, for the late calls at night, for the smiles...for your "Elda come on" ...And thanks Gabriel, for loving her and making her happy. And for making me always feel at home and for always having a smile in the face even if I know it is not easy to deal with a couple of twins.

Oscar, thanks for being the big brother, in all senses. For having always a word of support...and also some regrets . You're right. You have always been right with

your advices, even if I hadn't followed all of them (I should have done it more often). Thanks for make me have the feet on the floor and thanks you and Olga for giving me the best and lovely present in this world. Bruno, my nephew.

And Diego, for being you. Because I love you. Because you help me to believe in me. For everything (even the bad moments). Thanks for understand my needs and for never trying to stop me when following my dreams.

And the warmest thanks to the rest of my family...big and nice. Always there. The Spanish part: my grandma (Yaya, por ti va esto), my uncles Fede, Pilar, Rafa, Gina, my cousins Fede, Marta (Marta, thanks for our Tuesdays tea nights watching movies and talking), Youssef, Dani, Nuria, Jose, Monica, Laura and Rafa and its husbands and wives... and the Italian one: my uncles Cesarina, Mario, Rosanna, Enrico, Francesca, Emilio, Renato, Antonia and "zietta" Elda and my cousins an his sons, Monica, Lele, Lella, Paola, Lele, Andrea and Cristina. Thanks all of us and a special loving memory to the ones that are no longer there. Never forget.

Thanks to my friends, all over the world. Specially Ivan and Gemma, in Barcelona. Half of my degree is your fault. Thanks for being there always, with a glass of wine or with a handkerchief. Thanks for 'kicking my face' to make me keep going and for hug me when my strength was not enough. I've had used yours, so thanks for that. And thanks to you, Roser J., for bringing me back to reality.

Roser, (nena), thanks for picking me at the Renens VD station the first day I get to Lausanne. Thanks for your kindness and never ending happiness. For your smiles. For smoothing my way in Lausanne. For your place the first days. For making me realize how incredible are you. For everything, thanks.

Thanks my friends in Spain whereas in Madrid, Segovia, Barcelona, Canary Island...Carlitos, Luis, Juan, Javigo, Roberto, Manolo, Carlos, Fran, Sofia, Roman, Montse (specially you, Montse for having always time to listen to me in the bad moments without conditions), Jordi (for being an important part of life for some years, and even now), Vega, Arnau...and many more. Thanks everyone.

And finally, I would like to thank to the "spanish clan". The good people I met in Lausanne: Anna ("pels cafetons de mitja tarda i cotilleos varis"), Lluís, Luis, Cesar, Javi, Xavi (again), Rafa, Sara B., Oriol, Virginia, Jose, Luigi (even if you're not spaniard). Thank you for your support and for the good moments. Lots of pictures but specially, lot of remembers.

And Sara, you're coming apart. I owe it to you. Actually, it is strange, but knowing you had been one of the most amazing thinks in my life. Almost the same, but different, you have always been there. Even if the situation was neither easy for you. Thanks for that. Thanks for being my biggest support here, in Lausanne. For always answering the phone, for always listening to me. For your advices...and for the moments of joy and laughs. For giving me the best moments in Lausanne. For make me laugh until cry...thanks for everything.

My most sincere thanks to everyone, even the ones I've forgotten when writing this. This work is also yours.

*Si el mundo se te ha quedado pequeño  
abre tus alas y echa a volar*

# Contents

<b>1</b>	<b>Introduction</b>	<b>1</b>
1.1	Motivation of this work . . . . .	1
1.2	Goals of this project . . . . .	2
<b>2</b>	<b>MRI Acquisition Fundamentals</b>	<b>5</b>
2.1	MR Physics . . . . .	5
2.2	Excitation . . . . .	8
2.3	Signal Reception . . . . .	9
2.4	Image Reconstruction . . . . .	11
2.5	Fundamental MRI Acquisition Methods . . . . .	11
2.5.1	FLASH acquisition . . . . .	12
2.5.2	MPRAGE acquisition . . . . .	13
2.6	Field Dependence of MR Imaging Parameters . . . . .	15
2.7	Summary of MR Acquisition Fundamentals . . . . .	16
<b>3</b>	<b>Analysis of the Bias Field</b>	<b>18</b>
3.1	Mathematical approach for a MR image . . . . .	19
3.2	Tissue Signal Distribution . . . . .	21
3.3	The Noise in MRI . . . . .	22
3.4	Bias Field in Low-Field Acquisitions . . . . .	24
3.5	Drawbacks when Increasing Field Strength . . . . .	25
3.6	Bias Field in High-Field Acquisitions . . . . .	27
3.7	Summary of Analysis of Bias Field . . . . .	30
<b>4</b>	<b>State-of-the-Art Methods for Bias Correction</b>	<b>31</b>
4.1	Prospective and Retrospective Methods . . . . .	31
4.1.1	Prospective Methods . . . . .	32
4.1.2	Retrospective Methods . . . . .	33
4.2	Summary of State-of-the-Art Methods for Bias Correction . . . . .	35
<b>5</b>	<b>Analysis of Retrospective Methods</b>	<b>37</b>
5.1	The Parametric Bias Correction (PABIC) . . . . .	37
5.2	Results and validation of PABIC Method . . . . .	39
5.2.1	Correcting a 2D Human Brain Image . . . . .	40
5.2.2	Correcting a 3D Human Brain Image . . . . .	44
5.3	The Low Pass Filter Correction . . . . .	45
5.3.1	Results and Validation of the Method . . . . .	49
5.3.2	Summary of Bias Correction with Retrospective Methods . . . . .	51

<b>6</b>	<b>A New Prospective Solution Using the RF Mapping</b>	<b>53</b>
6.1	Magnitude $B_1$ Mapping and Flip Angle Mapping . . . . .	55
6.2	Bias Correction using the RF Mapping . . . . .	57
6.3	Results and Validation of the Method . . . . .	57
6.4	Summary of A New Prospective Solution Using the RF Mapping . .	60
<b>7</b>	<b>Conclusions and Future Work</b>	<b>61</b>
<b>A</b>	<b>Radio-frequency Power Requirements of Human MRI</b>	<b>63</b>
A.1	Power an SAR Calculations . . . . .	63
<b>B</b>	<b>1D Electromagnetic (EM) Theory for Wave Interference</b>	<b>64</b>
<b>C</b>	<b>Relative Spatial Phase Patterns for Received and Transmitted <math>B_1</math> Field</b>	<b>66</b>
<b>D</b>	<b>Legendre Polynomials</b>	<b>68</b>
<b>E</b>	<b>Optimization with (1+1)-ES algorithm</b>	<b>69</b>

# Chapter 1

## Introduction

### 1.1 Motivation of this work

Human diseases diagnosis has been one of the principal goals in medicine. Since the beginning of the modern Medicine, all the research has been focused on finding the causes of the diseases and its cures by understanding human body behavior. In the case of the neurological research, this idea has been translated in finding the way of studying the brain in the harmless way.

Since its first days, MR technology has demonstrated to be the best and more reliable way to study inner tissues of human body, specially the brain. Indeed, it is considered the harmless and most potent way for giving and accurately insight into the physiological condition of the brain.

Much have been done in the field of the MRI acquisition at lower fields but not at higher fields. In fact, clinical systems had improved since the first ones developed in early 80's increasing field strength from  $0.2T$  over  $1.5T$  and  $3.0T$  with specially good results in **contrast** and **image resolution** in human brain imaging. But, the final target in the history of clinical MR has always been moving to ever higher magnetic field strength. In point of fact, increasing the main field strength allow us to get advantage of a better **signal-to-noise ratio** (which increases almost linearly with the field strength [27]). This improvement of the **SNR** allows higher spatial resolution and/or faster imaging, a greater spectral dispersion, as well as an enhanced sensitivity to magnetic susceptibility. Its potential has been cleared demonstrated for high resolution imaging of the brain microvasculature [1], [9], brain spectroscopy [20], and functional MRI (fMRI).

It has been with the demand of reliable measurements of MR parameters in the diagnosis and prognosis of disease, that has been placed increased importance on the accuracy and precision of MR imaging technique. In fact, in the last decade, MRI studies conducted at  $4T$  have demonstrate the utility of **high magnetic fields** in anatomical imaging of the human brain. If we take also into account the great and continuous successful results obtained at magnetic field up to  $9.4T$  with animals models [40], we can conclude we find ourselves in the best scenario for the exploration of magnetic field of higher than  $4T$  for human brain studies. Following that aim, the technology for **high field human MR** research, which describes experiences with  $7T$ ,  $8T$  and  $9.4T$ , is crossing the boundary to the clinical issues as most of the drawbacks of this methodology had been solved and it is almost ready to address clinical issues. The simply reason is that having the chance of giving an

accurate insight into the physiological condition of the brain can help, not only as it can might be thought, in tumoral diseases diagnose, but also in the diagnose and prognosis of less known diseases as *Alzheimer* or *Senile Dementia*.

The main drawback when increasing magnetic field intensity in MR imaging is that, doing so, it also increases the so-called **Intensity Inhomogeneity** or **bias field** which makes specially difficult most of the medical proceedings for diagnosis, such as the tissue-segmentation or even a visual inspection, affecting the quantitative image analysis.

In **low field acquisition**, that is to say, fields from intensity less or equal  $3$  *Tesla*, the bias field associated to the MRI acquisition had already been defined. As it can be considerate **smooth** and with a **slow time variation** it can be mathematically modeled by smooth functions such as the *Legendre polynomials*, or just removed by low-pass filtering. The *PABIC*, *PARametric BIAs COrrrection*, mainly developed by Martin Styner [31], has been largely tested in MRI acquisitions of  $1.5$  *T* with optimal results in *bias field correction*.

But if we increase the applied main field, we find unsuitable effects or artifacts that cannot be treated as we have been doing with low-field acquisitions. In fact, when increasing field strength (specially if we work with **high field acquisitions** ( $> 7T$ )), the bias field starts having a **wave behavior** that makes impossible its approximation by an smooth function as it is strongly dependent in the dielectric effects, and the conductivity of each tissue in the brain.

During this report we will focus in this *wave behavior* of the *bias field*, giving a method that could (at least partially) erase it from the original image increasing contrast and image resolution. This work is divided in several chapters. The Chapter 2 is focused in MRI acquisition process giving an explanation about physics' background of this imaging mechanism and the different types of acquisitions we can obtain while changing parameters in the acquisition pipeline. In the next Chapter, chapter number 3, we will define the bias field approximation either for low field acquisition than high field ones, giving the main drawbacks when increasing the main field strength. After that, we will start talking about the *state-of-the-art methods* in bias correction, making difference between the prospective methods and retrospective ones. This will be in Chapter 4. After having sorted all the methods developed for achieve bias correction, some test had been performed. With this test, we want to prove that the main methods used until this moment are not enough valid for successfully correct MR image acquisition with field higher than  $3T$ . The results are shown in Chapter 5. Is in Chapter 6 where we propose a method of bias correction based on the acquisition (at the same time that the high contrast image) of a **RF map**, which give us the representation of the bias field in the moment of the acquisition. The conclusion and the future work are presented in the last Chapter of the report, defining a possible line of work for posterior studies of bias field correction in  $7T$  MR imaging.

## 1.2 Goals of this project

The aim of this project is to remove the bias distortion, so called *bias field* or *intensity inhomogeneity*, from MRI images of human brain acquired with  $7T$  MR machines. The images have been supplied by the *CIBM*, *Centre d'Imagerie Biomedicale* ([www.CIBM.ch](http://www.CIBM.ch)) which is a collaboration of the *Ecole Polytechnique Federale de Lausanne (EPFL)* with *L'Université de Geneve (UNIGE)*, *L'Université*

de Lausanne (UNIL) and its associated research and teaching hospitals (CHUV and HUG) in Switzerland.

This work has been done in collaboration with the **Siemens Development and Research Group** at the CIBM ([www.cibm.ch](http://www.cibm.ch)). The images had been acquired with a Siemens 7T machine sited at the CIBM, EPFL.

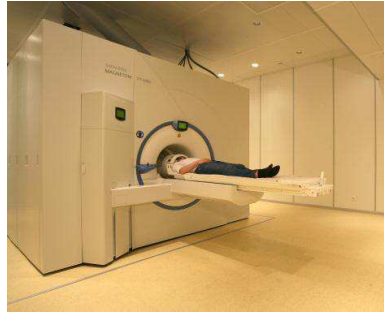


Figure 1.1: Siemens MAGNET for 7 Tesla acquisitions

Its technical characteristics are:

- MAGNET: Magnex Scientific 7 Tesla / 680 mm Bore Active shielded Ultra short length Zero boilloff magnet
- Cryostat length: 2200 mm
- Cryostat diameter: 2700 mm
- Cryostat weight (excluding cryogenes): 28 Tonnes approx.
- Nominal operating current: 192 Amps
- Energy stored: 39.3 MJ
- Console: Siemens

The ultimate goal is, obviously, to supply the medical community with a tool which can allow them to diagnose, in a reliable way, possible human brain diseases as well as help them understand its behavior.

There are several ways of improving MR imaging depending in the segment of the acquisition process in which we want to focus. Even if the aim of this work is to tackle the *inhomogeneity* problem focusing on improving **postprocessing** and **image reconstruction algorithms** some work had been done in the acquisition segment. Actually, a technique which uses the combination of both working lines, seems to be more appropriate for the success in brain imaging at *7 Tesla*, which, nowadays, is becoming a *Gold Standard* in Medical Research Institutes all over the world.

The main contribution of this master thesis is demonstrate that the methods for performing bias field correction in acquisitions with field less than  $3T$  are no longer useful for correcting  $7T$  acquisitions. All the conclusions and results we will shown in this master thesis are based in the fact that at  $7T$  the bias can not be assumed as a slow and smooth variation. This report focus in MRI acquisition of human brains images, but actually, the bias appears in all MR imaging techniques, whereas we

are imaging the brain or other parts of the body. So that, the conclusion we will assess for the specific case of the brain, can be extrapolate to other MR images.

This is my little contribution to this work. My one's bit part of it.

## Chapter 2

# MRI Acquisition Fundamentals

During this report, we will be dealing with several magnitudes and parameters of the MRI acquisition process. Is for that reason that we are starting this lecture with a little introduction to the MRI experiment just giving a context to facilitate the comprehension of the text.

Let us start providing general background information about several technical aspects of MRI which will be used as the basis of further chapters. It wil also help the reader understand the MRI acquisition process and its principles.

### 2.1 MR Physics

The MR imaging is based in an harmless natural process at the atomic level such as the modification of **proton spin** by magnetic fields or radio-frequency pulses. The signal then generated can be registered and evaluated by computer-aided image processing systems MR imaging, giving as a result an image with different types of contrast depending on the acquisition parameters used. But, what is the spin? Why is specially useful in MRI imaging?

Each biological body (that is to say, each living tissue) is rich in water (and therefore, hydrogen) whose nucleus is composed by one proton. This proton is a particle that has fundamental properties like charge, mass and spin and is this last one, the spin, the one used in MRI acquisition process.

**Spin** is a quantum number and it can be thought as ”**magnetic moment**”. Each individual unpaired nuclear particle possess a spin of 1/2 and can have positive (+) or negative (-) sign, which means that two or more spins can be paired together in order to erase the net spin. Only nuclei with odd number of particles can have a non-zero spin so that it can interact with external magnetic field by aligning themselves along/against the field. When placed in a magnetic field of strength B, a particle with a net spin different to zero can absorb a photon of frequency. This the principle of MRI.

The magnetic dipole moment for a spin  $\mu$  is given by

$$\mu = -\gamma \cdot \mathbf{S} = \gamma \hbar \cdot \mathbf{I}, \quad (2.1)$$

where  $\mathbf{S}$  is the spin angular momentum and  $\mathbf{I}$  is the spin. The constant  $\gamma$  is the gyromagnetic ratio and its value depends on the element (in the hydrogen case equals about  $42.6\text{MHz/T}$ ). Spins are in lower energy state when aligned in the same direction of the external field and in a higher energy state when they are aligned in the opposite direction. The specially useful quality of particles with spin is that they can undergo transitions between the energy states by absorbing (or releasing) photons with energy

$$E = h \cdot \nu, \quad (2.2)$$

where  $h$  is the Planck's constant and  $\nu$  is the frequency of the photon. In the case of MRI experiments this frequency is also seen as the "resonance frequency" called the **Lamor frequency**, which can be rewrite as

$$\nu = \frac{\omega}{2 \cdot \pi} = \frac{\gamma}{2 \cdot \pi} \cdot B_0. \quad (2.3)$$

The energy and the spin temperature determine the ratio between the number of particles in the lower energy state  $N^-$  and the higher state  $N^+$ ,

$$\frac{N^-}{N^+} = \exp(-E/kT), \quad (2.4)$$

and it is the difference between those two elements that cause the magnetization of the object thus, the local magnetic dipole moment per unit of volume:

$$M = \sum \mu. \quad (2.5)$$

The hydrogen nuclei interact with three types of magnetic fields in the MRI experiment:

- $B_0$ , the main magnetic field.
- $B_1$ , the excitation RF (radiofrequency) field.
- $G$ , the gradient field.

and is depending on the interaction with those fields that we can define different magnetization moments. In **static magnetic field**, if there's no other magnetic field, the net magnetization vector will have the same direction of  $B_0$ , that we usually assign at the  $z$  direction. This magnetization is called the **equilibrium magnetization** ( $M_0$ ).

The  $B_1$  **field** or **radio-frequency field** is generated by the RF coil and applied over the  $xy$  axis and its strength depends on the power transmitted per time value. When an excitation RF field is added at the Lamor frequency, the equilibrium of the tissue net spin is broken and the magnetization is tipped away from the  $z$  direction at an angle of certain degree. It will rotate about the  $z$  direction at the Lamor frequency and, eventually, come back to the equilibrium state. This recovery process of the magnetization along the  $z$  axis is called **longitudinal magnetization** ( $M_z$ ) and is characterized by an exponential curve with a time constant  $T_1$ . In the same way, the recovery process along the  $xy$  axis is called the **transverse magnetization** ( $M_{xy}$ ) and is characterized by the time constant  $T_2$  (as it also follows an exponential curve). In fact, this process is due to the fact that the spins loose phase coherence and start canceling each other out. Is not a complicate proceeding; when starting the MRI experiment, the spins rotating at Lamor frequency have zero phase. After  $TE/2$ , considering **TE** the **echo time**, some spins will rotate faster than the Lamor frequency and they will accumulate

a positive phase difference equals  $\sin(\omega + \phi \cdot TE/2)$ . On the other hand, we can found, also, spins which rotate slower than the Lamor frequency, so its phase difference will be  $\sin(\omega - \phi \cdot TE/2)$ . Is at the time **TE** when they will be in phase again. The transition back to equilibrium after a perturbation is called **relaxation**.

The **longitudinal magnetization** behavior is defined by:

$$\frac{dM_z}{dt} = \frac{M_z - M_0}{T_1}, \quad (2.6)$$

and given the initial condition  $M_z(0)$ , the solution of this equation can be written as

$$M_z = M_0 \cdot (1 - \exp(\frac{-t}{T_1})), \quad (2.7)$$

where  $T_1$  is the **spin-lattice relaxation time constant** of the imaging sample. Its value is typically longer at high field strengths whereas in lower fields is smaller as  $M_z$  takes longer to recover.

The **transverse relaxation**, also called **spin-spin relaxation** follows the equation

$$\frac{dM_{xy}}{dt} = \frac{M_{xy}}{T_2}, \quad (2.8)$$

and can be solved giving the result

$$M_{xy} = M_0 \cdot \exp(\frac{-t}{T_2}), \quad (2.9)$$

where  $T_2$  is the **spin-spin time constant**. The  $T_2$  in tissue is independent of field strength because its decay is due to the phase coherence's lost.

The two relaxations occurs simultaneously and the  $T_2$  value is always smaller (or equal at least) than  $T_1$ . The problem is that in MRI experiments is hard to see the pure  $T_2$  effects because it is due to both spin interactions and the  $B_0$  inhomogeneity. For study this double dependence we use the **combined time constant**, called  $T_2^*$  who can we expressed as

$$\frac{1}{T_2^*} = \frac{1}{T_2} + \frac{1}{T_2'}, \quad (2.10)$$

where  $T_2'$  is called *susceptibility*. In fact we can assume that  $T_2^*$  decay is due to local inhomogeneities which can be re-phases and the tissue properties (spin-spin interactions, different structures in the brain such as bones, cartilages and cerebrospinal fluid). In figure 2.1 we can see an example of this relaxation times depending on the protocol used for acquiring the image. .

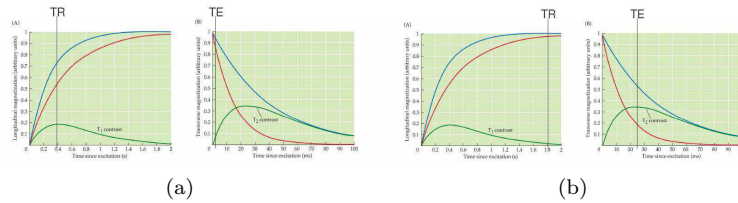


Figure 2.1: Longitudinal magnetization and transverse magnetization values for a T1-weighted (a), and T2-weighted (b) images

The **gradient field** is a compound of linearly variations of the intensity of the main magnetic field depending of the space, which are transitory added. This addition is done in order to localize the signals that belong to each voxel, as these gradients induce attractions and rejection moments between the coils. Each type of image obtained by MR experiments (EPI, gradient echo, ...) uses an specific combination of this gradients. In the section *Fundamental Acquisition Methods* of this Chapter we will focus in this property of the gradient fields.

In resume, we have to deal with several external magnetic field interactions and with different relaxations times for the precession motion of the hydrogen spins inside the tissues. But, how can we deal with this all together?

For describe the *motion of the magnetization vector due to all the external magnetic influences*, we use the **Block equation**. This equation can be used in any condition and it *relates the effect of the combined magnetic fields in the sample and the relaxation times of its tissues*. It can be described as follows:

$$\frac{d\vec{M}}{dt} = \gamma \cdot \vec{M} \times \vec{B} - \frac{-M_x \vec{i} + M_y \vec{j}}{T_2} - \frac{(M'_z - M_0) \vec{k}}{T_1}, \quad (2.11)$$

On right hand, the first term ( $\gamma \cdot \vec{M} \times \vec{B}$ ) describes the free precession without considering  $T_1$  and  $T_2$  effects whereas the second term ( $-\frac{-M_x \vec{i} + M_y \vec{j}}{T_2}$ ) is the  $T_2$  effect and the third ( $-\frac{(M'_z - M_0) \vec{k}}{T_1}$ ) is the  $T_1$  effects on the magnetization vectors.

## 2.2 Excitation

The excitation process is the way to establish the phase coherence of individual magnetic moments, in order to generate a transverse magnetization. In fact, when the tissue is in the equilibrium state (that is, only influenced by a external static magnetic field  $B_0$ ), there is not any transverse magnetization because all the phases are canceled with each other. Is for that reason, that an external force must be applied at the spin system.

This force is the RF field  $B_1$ , generated at the RF coils, which is an oscillating field perpendicular to the main field. The rotation of this  $B_1$  field is at the Lamor frequency so that the energy exchange can be facilitate.

The  $B_1$  is normally a RF pulse and can be described by a sinusoidal function:

$$\vec{B}_1(t) = 2\vec{B}_{1e}(t) \cos(\omega_r f t), \quad (2.12)$$

where  $\vec{B}_{1e}(t)$  modulates the amplitude and  $\omega_r f$  is the carrier of the RF pulse. If we rewrite the expression using complex notation we obtain:

$$\vec{B}_1(t) = \vec{B}_{1e}(t) \exp(j\omega_r f t) + \vec{B}_{1e}(t) \exp(-j\omega_r f t). \quad (2.13)$$

So we can distinguish two rotating components. One is clockwise, and is called  $B_1^+$  and the other, called  $B_1^-$  is counterclockwise component. We will see in Chapter 3 (where we will do an analysis of the bias field) that in **low field approximation**, the counterclockwise rotating component is not used to compute the field as is almost negligible in front of the clockwise rotating component. This assumption could not be done in the **high field approximation** and this fact will direct us

to one (and the most important) drawback on bias field approximation at high fields.

Coming back to our topic, we can find two types of excitation depending on if the RF pulse is tuned or not at the Lamor frequency of the main static field. The **on-resonance excitation** assumes that there is a constant Lamor frequency (or uniform  $B_0$  field) so the RF pulse can be easily tuned at the same frequency. When do that, a phase coherence of spin is established. A transverse magnetization emerges and the  $B_1$  field get aligned along the  $z$  axis. The condition to have **on-resonance excitation** is

$$\omega_{rf} = \omega_0 = \gamma B_0. \quad (2.14)$$

The effect of the  $B_0$  field is offset by the carrier frequency of the RF pulse. The only observed magnetic field is the  $B_{1e}$ . Is for that reason that a much smaller  $B_1$  (if we compare it with the main field) can flip the magnetization away from the direction of the much stronger  $B_0$  field. The angular frequency of that rotation is:

$$\omega_1 = \gamma B_0. \quad (2.15)$$

Calculating the time integral over the duration of the pulse  $T$  of the angular frequency rotation, we can compute the **flip angle**

$$\alpha = \int_0^T \omega_1(\tau) d\tau = \gamma \int_0^T B_1 e(\tau) d\tau. \quad (2.16)$$

For a rectangular RF pulse, solving the integral, we get

$$\alpha = \omega_1 T = \gamma B_1 e T. \quad (2.17)$$

The problem when tuning the RF pulse is that in real cases the  $B_0$  is not perfectly uniform in the whole volume, which means the  $B_0$  is a kind of variational function, so the RF pulse cannot be perfectly tuned to it. The difference between the local  $B_0$  field with the supposed Lamor frequency to which the RF is tuned to is called **off-resonance excitation**. This produces a phase shift. This de-phasing effect caused by the off-resonance is characterized by the  $T_2$  equation (2.10).

## 2.3 Signal Reception

As we have seen in the previous sections of this Chapter, after the tissue has been excited, its spins will precess at the Lamor frequency so we can detect this motion with a coil. This is the basis of MRI phenomenon. In fact, as **Faraday** state in his law, a time-varying field will induce a voltage in a coil placed perpendicular to the direction of the magnetic field. This statement is known as the *Faraday's Law*. Mathematically it is represented as

$$V = -\frac{\partial \Phi(t)}{dt}, \quad (2.18)$$

where  $\Phi$  is the magnetic flux. So, if we take in account the **Reciprocity Principle**, we can determine this flux in the coil. If a current flows in the coil, it will produce a magnetic field  $B^r(r)$  at location  $r$ . Thus, the magnetic flux throw the coil will be

$$\Phi(t) = \int \mathbf{B}^r(r) \cdot \mathbf{M}(r, t) dr. \quad (2.19)$$

If we replace this value in equation 2.18, we finally obtain the expression of the voltage induced in the coil

$$V = -\frac{\partial\Phi}{\partial t} \int \mathbf{B}^r(\mathbf{r}) \cdot \mathbf{M}(\mathbf{r}, t) d\mathbf{r}. \quad (2.20)$$

The  $z$  component of the magnetization  $M$  is parallel to the plane of the coil so we can ignore the component  $M_z$ , keeping only the  $M_{xy}$  component. Is for that reason that many times the MR signal is often named transverse magnetization. But we don't record this signal. The signal we record is usually the voltage after the demodulation of the high frequency term, and is represented as

$$S(t) \propto \omega_0 \int \mathbf{B}_{xy}^{r*} * \mathbf{M}_{xy}(\mathbf{r}, 0) \exp\left(\frac{-t}{T_2(\mathbf{r})}\right) \exp(-j\Delta\omega(\mathbf{r})t) d\mathbf{r}, \quad (2.21)$$

where  $B_{xy}^{r*}$  is the complex conjugate of the transverse received magnetic field  $B_{xy}^{r*}$ , named the **receive coil sensitivity**.

If we reject the  $T_2^*$  effects, we have that the signal amplitude is proportional to (1) the Lamor frequency, (2) to the coil sensitivity, (3) the transverse magnetization, and finally,(4) to the sample volume. And, as the Lamor frequency is linearly related to the main magnetic field, we can say that we will supposedly have an improvement on the **signal-to-noise ratio (SNR)** when increasing the main field.

The signal equation derived can be directly applied in **Free Induction Decay** experiments, which are normally used to optimize MRI systems. In this experiments, the signal is collected after the RF pulse is applied. No gradient fields are involved there.

However, spatial information can be encoded during the free decay period by adding a gradient magnetic field over the main field. It can be done in two different ways, giving us the (1) **frequency encoding** and the (2) **phase encoding**.

The **frequency encoding** was first proposed by *Lauterbur et al.* in 1973 [19]. Adding a gradient field along an arbitrary line  $\mathbf{r}$  in the space we can establish a linear relationship between spatial information along  $\mathbf{r}$  and the frequencies of the MR signal. In this case, the Lamor frequency at  $\mathbf{r}$  is:

$$\omega(r) = \omega_0 = \gamma G_{FE} r, \quad (2.22)$$

so after removing the center frequency  $\omega_0$  and without considering the  $T_2$  effects and the coil sensitivity effects qwe can get to the following expression for the signal intensity

$$S(t) \propto \int_{-\infty}^{\infty} M(r) \exp(-j\gamma G_{FE} r t) dr. \quad (2.23)$$

To generate a multidimensional image, we also need to use the **phase encoding**.

The **phase encoding method** encodes the spatial location with different initial phases. A gradient field along a line  $r$  is turned on for a short period of time, and then turned off. The signal after a period  $(T_P)_E$  is

$$S(t) \propto \int_{-\infty}^{\infty} M(r) \exp(-j\gamma G_{PE} r T_{PE}) dr. \quad (2.24)$$

Combining the frequency and phase encoding methods , we can encode a  $2D$  and  $3D$  space in arbitrary coordinate.

## 2.4 Image Reconstruction

At this point, we have a **raw signal** that we need to transform into an image. There is a Fourier relationship between the raw signal and the MR image. In fact, looking at the equation 2.24 we can consider its phase term as

$$\phi = -j\gamma \int_0^t \mathbf{G}_r(s) \mathbf{r} ds, \quad (2.25)$$

so that allow us to define a **k-space** as

$$\mathbf{k}_r(t) = \frac{\gamma}{2\pi} \int_0^t \mathbf{G}_r(s) ds. \quad (2.26)$$

Thus the signal is just the Fourier transform of the magnetization.

$$S(\mathbf{k}_r) = \int_{-\infty}^{\infty} M(\mathbf{r}) \exp(-j2\pi\mathbf{k}_r\mathbf{r}) d\mathbf{r}. \quad (2.27)$$

These equations mean that the k-space coordinates are determined by the area under the gradient waveform.

The **k-space** is also called the *spatial frequency space*. It is the conjugate of the image space. Computing the **Fourier transform** of this space is how we generate the MR image. Thus, we can say the *k-space* is the temporary place where the raw data is stored. When this space is full, a *FFT* is computed transforming the *k-space* data into the *r-space* or Euclidean space where we will proceed at the signal processing. In fact, the raw data contains the frequency information and, when applying the Fourier transform we obtain the spatial information we will process.

## 2.5 Fundamental MRI Acquisition Methods

Depending on the way the signal has been generated, we have different types of MRI images, that is to say, image contrasts. We can consider two main groups in MR acquisition methods, the (1) **spin echo imaging (SE)** and the (2) **gradient echo imaging (GE)**. In the figure below they are been roughly listed:

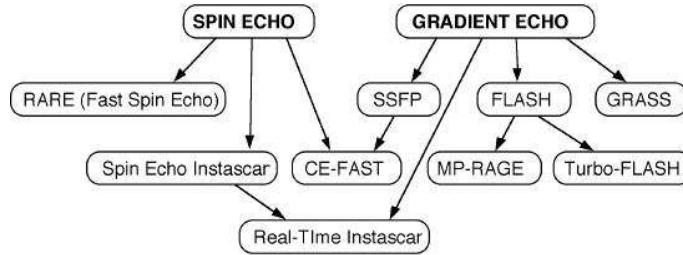


Figure 2.2: Types of MRI acquisition

The mechanisms used for generate the signal in each case are different. In the **gradient echo imaging**, signal is generated by magnetic field refocusing mechanism only. This mechanism is specially used to measure de  $T_2$  value of the tissue as it reflects the uniformity of the magnetic field.

The signal intensity in *gradient echo* images is governed by

$$S = S_0 \exp\left(\frac{-T_E}{T_{2^*}}\right), \quad (2.28)$$

where  $T_E$  is the **echo time** or time from the excitation to the center of the  $k$ -space.

For the **spin echo**, the signal is generated by a radio-frequency pulse refocusing mechanism (using and 180 degrees pulse). This image contrast doesn't reflects the uniformity of the magnetic field (instead of *gradient echo imaging*), as it does not take into account the  $T_{2^*}$  value but  $T_2$ . The signal in a *spin echo acquisition* is governed by the equation

$$S = S_0 \exp\left(\frac{-T_E}{T_2}\right). \quad (2.29)$$

In both cases we can achieve a **fast imaging**. In principle, the *fast imaging* is a technique that can generate an entire image by sub-second temporal resolution. In this technique, steps are taken to destroy any residual transverse magnetization prior to each excitatory RF pulse. In this way, only longitudinal magnetization is incorporated into the steady state.

### 2.5.1 FLASH acquisition

In **FLASH**, after the signal is collected in the form of a gradient echo, a gradient pulse called a "spoiler" is used to destroy any remaining transverse magnetization. From there, the magnetization recovers longitudinally at the tissue  $T_1$  rate. The brevity of the  $T_R$  (**repetition time**) in *FLASH* necessitates the use of a spoiler; without it, some transverse magnetization would remain at the beginning of the next RF pulse.

It provides a mechanism for gaining extremely high  $T_1$  contrast by imaging with  $T_R$  times as brief as 20 to 30msec while retaining reasonable signal levels, as extremely short  $T_R$  times are not possible with the conventional SE technique. In fact, the presence of a 180 pulse in SE pulse sequences results in a loss of signal as the  $T_R$  becomes small compared to the  $T_E$ . In *FLASH acquisition*,  $T_2^*$  contrast is substituted for T2 contrast as the  $T_E$  is increased. The signal obtained by a Flash acquisition can be expressed as:

$$SI = \frac{(1 - \exp(\frac{-T_R}{T_1})) \cdot \exp(\frac{-T_E}{T_{2^*}})}{1 - \cos(\theta) \cdot \exp(\frac{T_R}{T_1})} \cdot \sin(\theta). \quad (2.30)$$

The FLASH image has less contrast than the MPRAGE acquisition, but, on the other hand, it is easily acquired and the time lasted for iis smaller than the needed for a complete MPRAGE acquisition. In figure 2.3 we have an example of a FLASH acquisition.

Let's clarify the different views we get from a MR image. **Transverse** view is the one we get from underneath. The first section (or slice of the volume) is the

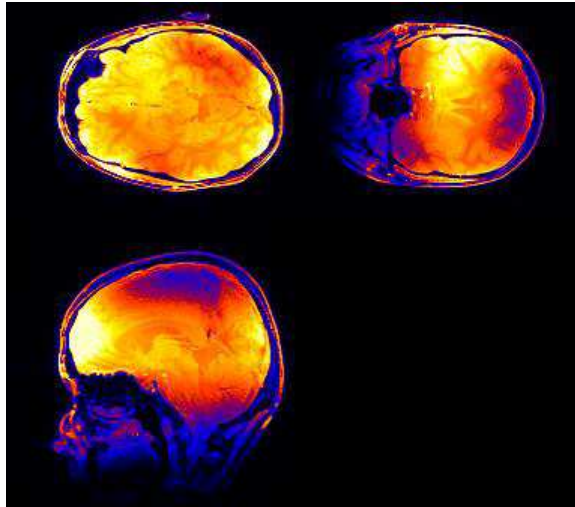


Figure 2.3: Transverse, sagittal and coronal view of a FLASH acquisition at  $7T$  of a human brain

most inferior (bottom). **Sagittal** view is from right side (and of course, first section is the right side), and finally, **Coronal** view is from front. In this case, the first section (or slice) is the most posterior (the back one).

## 2.5.2 MPRAGE acquisition

Because the acquisition times in these *ultra-fast FLASH* images are comparable to, or less than, tissue  $T_1$ 's, one plausible strategy for improving contrast is to precede the acquisition with one or more "preparation pulses" (leading to the acronym **MP-RAGE** for *Magnetization-Prepared Rapid Acquisition with Gradient Echoes*) so that the longitudinal steady state, prior to the FLASH acquisition, is altered. Typical preparatory sequences might be an *inversion ( $180^\circ$ ) pulse* to add  $T_1$  contrast, or a  $90^\circ - 180^\circ - 90^\circ$  series to add  $T_2$  contrast. When the acquisition time is comparable to, or longer than, the tissue  $T_1$ , this can lead to some contrast anomalies as the signal changes during sampling. To compensate for this effect, some investigators have suggested partitioning the data collection into segments, each having a relatively short duration, separated by a recovery period and an additional preparation pulse.

**MPRAGE** acquisition (*MP-GRE / MPRAGE / MP-RAGE*) is a fast *3D gradient echo pulse sequence* that uses a magnetization preparation pulse like *Turbo FLASH*. Only one segment or partition of a 3D data record is obtained per inversion preparation pulse. After the acquisition, for all rows a delay time ( $T_D$ ) is used to prevent saturation effects. *MPRAGE* is designed for rapid acquisition with  $T_1$  weighted dominance. Fast gradient echoes are characterized by their rapid sampling time, high signal intensity and image contrast while approaching steady state (the echo is collected during the time when tissues are experiencing  $T_1$  relaxation).  $T_1$  weighted three-dimensional MPRAGE sequences are used to obtain structural brain scans. Following an inversion pulse and delay  $T_1$ , a single segment of a 3D-Gradient Echo (GRE) image is acquired. After further relaxation delay  $T_D$ , this process is repeated for next segment. However, there is a major drawback *MP-RAGE* imaging when many partitions are selected. This is the lost of contrast during the segment

acquisition due to relaxation effects.

As *Deichmann et al* assessed in [10], the image intensity in a MPRAGE acquisition is mainly determined by the value of the *longitudinal magnetization* available when the *central k-space lines* are acquired, so it depends on the **PE (Phase Encoding)** used. In **centric PE** the central k-space lines are acquired first (in the beginning of the acquisition block) whereas when **linear PE** is employed, half of the segment acquisition time has already passed when these lines are acquired (in fact these lines are acquired in the center of the acquisition block, when a partial  $T_1^*$  relaxation has already taken place). So, for centric PE, the signal strength is given by:

$$S_c = M_1 \cdot \sin \alpha, \quad (2.31)$$

While the signal strength when Linear PE is used can we written as:

$$SI = \{M_0^* + (M_1 - M_0^*) \exp(\frac{-\tau}{2T_1^*})\} \sin \theta, \quad (2.32)$$

with  $M_0^*$  the saturation value of  $M$  that can we developed as:

$$M_0^* = M_{(0)} \frac{(1 - \exp(\frac{-T_R}{T_1}))}{(1 - \exp(\frac{-T_R}{T_1^*}))}, \quad (2.33)$$

and  $T_1^*$  the time in which this saturation is reached than is expressed as:

$$T_1^* = [\frac{1}{T_1} - \frac{1}{T_R} \cdot \text{Ln}(\cos \theta)]^{-1}. \quad (2.34)$$

One example of a MPRAGE acquisition can be seen in figure 2.4: As we can see

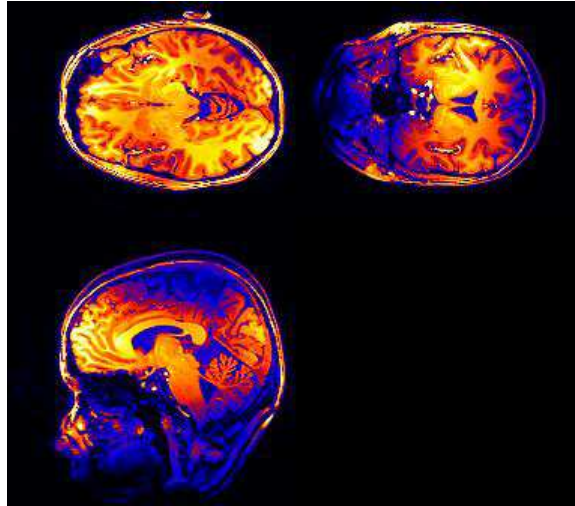


Figure 2.4: Transverse, sagittal and coronal view of a MPRAGE acquisition of a human brain

here, the contrast obtained is higher than thee one we get with a FLASH acquisition, but, otherwise, the bias artifacts are also stronger.

The main drawback of a *sequence based on centric PE* is its **vulnerability to RF inhomogeneities** as the contribution of the k-space lines to the image depends only to  $\sin \alpha$  since only the transverse component contributes to the signal. For that,

the strategy for bias compensation should be a first order compensation for RF inhomogeneity effects. In case of linear PE, this compensation requires the knowledge of the spatial dependence of the field amplitude  $B_1$  of the RF coil used. This fact is specially important. We will see that when increasing the field strength, the RF inhomogeneities became specially strong. This vulnerability will bring us to a bias image contrast, that we will try to enhance.

Otherwise, we have some acquisition methods that can achieve "such speed". Is the case of the **echo planar imaging**. **EPI** allows highest speed for dynamic contrast and is highly sensitive to the susceptibility-induced field changes. Besides, using *EPI* we can obtain an efficient and regular *k-space* coverage and a good **signal-to-noise** ratio. Even more, it can be applicable to most gradient hardware. In fact, the *SE* and *GE* methods take multiple RF shots to readout enough data to reconstruct a single image (each shot gets data with one value of phase encoding). But, if gradient system (that is to say, power supplies and gradient coil) are good enough, *EPI* can read out all data required for one image after one RF shot, so the total time in which signal is available is about  $2 \cdot T_2^*$  which is nearby  $80ms$ . This means it can acquire 10 – 20 *low resolution 2D images* per second.

## 2.6 Field Dependence of MR Imaging Parameters

We have been talking in the previous section about the MR imaging technique at its parameters. MR imaging is used to study inner tissues of the human body, and particularly of the brain. This work is focused in this last acquisition, MR imaging of human brain, but is useless to say that this study can be extended to whereas we are imaging the brain or other inner tissues in human body.

Human brain is a living load and the tissues present in it have kind of constant due to its dielectric and conductive behavior. For that, in this section we are making some further considerations in human brain imaging considering its physiological proprieties. We will try to explain the dependence of the main part of *MRI acquisition parameters* with the applied field.

Anatomical images of brain tissue rely on *Proton Density*,  $T_1$  and  $T_2$  differences between different regions (such as the cortex and the hypothalamus) and in the tissue types (white matter, gray matter and CSF). *Proton density* is clearly a magnetic field independent parameter [35]. In Chapter 2, we defined the proton density as the concentration of mobile Hydrogen atoms within a sample of tissue, so its clearly independent on the field applied to the sample (but not to the type of the tissue studied, of course).

Otherwise, *relaxation times*  $T_1$  and  $T_2$  are field dependent.  $T_1$  value generally increases with the increasing of the field whereas  $T_2$  decreases when the field increases. The conventional wisdom (in the previous stages of investigation with MR and its need to increase field strength), was that  $T_1$  value not only increases with higher magnetic fields but also we wish this value to converge the distribution of  $T_1$  among different tissues types would tend to become narrower, predicting a low contrast in the image. However, this hasn't shown to be true when increasing the field. In contrary, the distribution of  $T_1$  values among different types of tissues in the brain, including the difference between the cortical gray matter and adjacent superficial white matter increase with increasing magnetic field [35].

Following [35], the  $T_1$  value varies linearly with the field:

$$T_1 = 1.226 + 0.134B_0, \quad (2.35)$$

whereas  $T_2$  value decreases with increasing magnetic fields with a far linear drop. Exchange and/or diffusion on the presence of gradients may be the main responsible of this shortening.

SNR increases with increasing magnetic field strength, but its dependence with this field rise becomes complex due to the dielectric losses in biological samples. Some studies had been performed for the different SNR profile variations for  $4T$  up to  $7T$ . In [35], the SNR is shown to scale  $\sim 2$  fold more than linearly with field magnitude in the center of the image and less linearly in the periphery. However, at high field such as  $3T$ , SNR must be considered as a function of location within the head and specific coil geometries. Further considerations in power requirements and SAR values are done in Appendix A.3

## 2.7 Summary of MR Acquisition Fundamentals

Medical imaging refers to the techniques and processes used to create images of the human body (or parts thereof) for clinical purposes (medical procedures seeking to reveal, diagnose or examine disease) or medical science (including the study of normal anatomy and function). As a discipline and in its widest sense, it is part of biological imaging and incorporates radiology (in the wider sense), radiological sciences, endoscopy, (medical) thermography, medical photography and microscopy (e.g. for human pathological investigations). Measurement and recording techniques which are not primarily designed to produce images, such as electroencephalography (EEG) and magnetoencephalography (MEG) and others, but which produce data susceptible to be represented as maps (i.e. containing positional information), can be seen as forms of medical imaging.

This project will focus in one of these techniques, the MR imaging. A Magnetic Resonance Imaging instrument (MRI scanner) uses powerful magnets to polarize and excite hydrogen nuclei (single proton) in water molecules in human tissue, producing a detectable signal which is spatially encoded resulting in images of the body. In brief, MRI involves the use of three kinds of electromagnetic field: a very strong (of the order of units of teslas ( $T$ )) static magnetic field to polarize the hydrogen nuclei, called the *static field*; a weaker time-varying (of the order of 1 kHz) for spatial encoding, called the *gradient field(s)*; and a weak *radio-frequency (RF) field* for manipulation of the hydrogen nuclei to produce measurable signals, collected through an RF antenna. MRI traditionally creates a 2D image of a thin "slice" of the body and is therefore considered a tomographic imaging technique. Modern MRI instruments are capable of producing images in the form of 3D blocks, which may be considered a generalization of the single-slice, tomographic, concept. MRI does not involve the use of ionizing radiation and is therefore not associated with the same health hazards; for example there are no known long term effects of exposure to strong static fields and therefore there is no limit on the number of scans to which an individual can be subjected, in contrast with X-ray and CT. This factor, has not to be denied, as we will have a constraint when acquiring an MR image: the patient cannot be inside the magnet as much time as we need to have a perfect contrast, so the posterior digital processing of the image has to deal with this drawback. In fact, the higher the field applied is, the less time of acquisition time we have...but we get better contrast...We have here a compromise between time of acquisition and applied field. However, these risks are strictly controlled as

part of the design of the instrument and the scanning protocols used.

MRI being sensitive to different properties of the tissue, and while any nucleus with a net nuclear spin can be used, the proton of the hydrogen atom remains the most widely used, especially in the clinical setting, since it is so ubiquitous and returns much signal. This nucleus, present in water molecules, allows excellent soft-tissue contrast. Specially with the MPRAGE acquisition protocol.

This master thesis will focus on human brain acquisitions at  $7T$ . The images had been acquired following MPRAGE and FLASH protocols and had been supplied by the Siemens Research Group at the CIBM. Even though, it is useless to say that the conclusions assessed in this report can be extended to all kind of MR acquisitions (that is, acquisitions of any part of human body).

## Chapter 3

# Analysis of the Bias Field

In the previous chapters of this report, we have presented MRI acquisitions and its fundamentals and basis. And, doing so, we have slightly introduced the one of the drawbacks of any MRI acquisition, the *bias field*. This **inhomogeneous radio-frequency field**, added to the image, makes often impossible the differentiation between **gray matter** and **white matter** of the brain and lead us losing image contrast, making hard automated image processing techniques and even visual inspection. In fact, the bias makes the brightness of the image becomes not homogeneous along the brain.

The bias field (also termed as the intensity non-uniformity or intensity inhomogeneity IIN) usually refers to the slow, non-anatomic intensity variation of the same tissue over the image domain.

The strong bias field can be detected visually. Figure 3.1 can be a clear example of what kind of artifacts we can get due to the bias

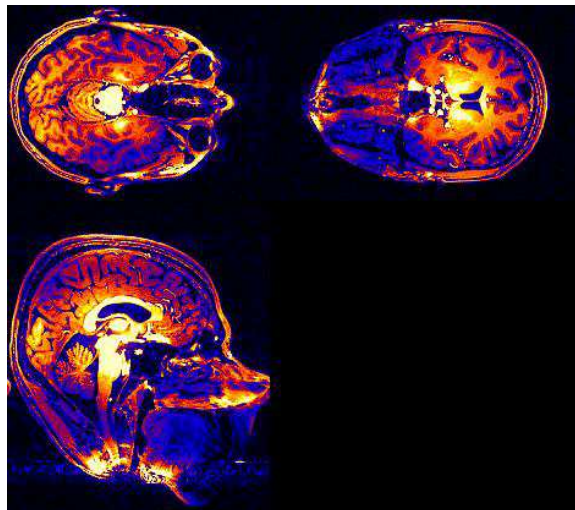


Figure 3.1: MPRAGE acquisition of a human brain corrupted by bias

In fact, if we look carefully we can see that in most part of the brain, specially in the frontal and temporal lobe, and the hypothalamus, we don't have much resolution (the edges between grey and white matter are no precisely defined) so in those points we can be considering that is white mater when is grey one, instead.

Besides, a part from the shifting between gray or white matter, in the image we can see bright spots in the center and in the frontal and backwards part of the image. Is, exactly, in the center of the image where we are supposed to have the best **Signal-to-Noise Ratio** but, in *7T acquisitions*, this region is the most corrupted by the *bias field*. Actually, due to this extremely high brightness, we are not able to discern none of the pixel values on it, and so, we cannot see this regions with enough precision to determine whether some disease or not.

In fact, the presence of IHH can significantly reduce the accuracy of image segmentation and registration, hence decreasing the reliability of subsequent quantitative measurements. Our main goal is to remove or at least reduce this artifact, giving a nice and clear insight view of all parts of the human brain.

### 3.1 Mathematical approach for a MR image

The generally accepted assumption on *intensity inhomogeneity* (for low-field acquisitions) is that it manifest itself as a *smooth spatially varying function that alters image intensities that otherwise would be constant for the same tissue type regardless of its position in the image*. In the most simple form, the model assumes that the intensity inhomogeneity is **multiplicative** or **additive** which means that the intensity inhomogeneity field multiplies or adds to the image intensities. [36]

Either on what is the source of the inhomogeneity we want to model, we use the multiplicative form or the additive. Most frequently, the multiplicative model has been used as it is more consistent with the inhomogeneities of the receiving coil but, for modeling the inhomogeneities due to induced currents and non-uniformity excitation the additive model is more suitable [29].

In addition to intensity inhomogeneities, the MR image formation model should include the noise, which is supposed to be at high-frequencies. This noise is known to have a *Rician distribution* even if, as the Signal-to-Noise ratio (SNR) is not too low, we can approximate it by a quasi-Gaussian (so, Rayleigh distribution) [28]. The next section is entirely devoted to the noise in MR acquisition, so we will focus on it later.

Different models of MR image formation has been proposed in the literature. The most common is the one that assumes an multiplicative bias field and an additive noise. But, how we get to the signal expression?

The image processing (as we have seen in Chapter 2) begins when all the MR information is stored in the *k-space*. When this space is full, the data is transformed onto the *r-space data* by simply computing an FFT [30], [23], [13]. Is when applying this FFT, when we get the spatial information needed for processing the image. In fact, the two distributions carry exactly the same information (even if the raw data, the one stored in the k-space, contains the frequency information). The transformation from one to the other is, following [30]:

$$\omega(r) = \int W(k) \exp(-2\pi j(kr)) dk. \quad (3.1)$$

So, after acquiring the signal and translate it into the *r-space*, this acquired signal

can be expressed as:

$$s(\underline{x}) = (o(\underline{x}) + n_{bio}(\underline{x})) * h(\underline{x}) + b(\underline{x}) + n_{RM}(\underline{x}), \quad (3.2)$$

where:

- $s(\underline{x})$  is the measured and digitalized data.<sup>1</sup>
- $\underline{x} = (x, y, z)$ .  $(x, y)$  are the spatial coordinates of each slice and  $z$  moves along the different slices.
- $o(\underline{x})$  is the ideal bias and noise free image.
- $n_{bio}(\underline{x})$  is the biological noise due to interior structures of the tissues, physiological noise, cardiac rate, respiration motion...
- $h(\underline{x})$  is the model of the blurred border region effect due to discrete sampling of the tissue.
- $n_{MR}$  is the noise due to the measuring devices acquisition.
- $b(\underline{x})$  is the added bias field (considering its value  $0 < b(\underline{x}) < 1$ ).

Considering how the signal intensity, the noise and the bias field interact, we can find some easier approximations, which lead us to the same results without making any assumption about the value of  $h(\underline{x})$ . Even if two sources of noise are described in the signal form (the biological one which corresponds to the within tissue inhomogeneity and the scanner noise that arises from MR devices imperfections), usually only one of this sources is modeled [36]. The most common model assumes that the noise, with a Gaussian distribution, arises exclusively from the scanner and is therefore independent from the bias field. So, following this model, the acquired signal can be approximated as:

$$s(\underline{x}) = o(\underline{x})b(\underline{x}) + n_{RM}(\underline{x}). \quad (3.3)$$

If we consider that only the biological noise interacts in the image formation, we get another expression for the obtained signal, where the ideal signal  $o(\underline{x})$  and the noise  $n_{bio}(\underline{x})$  are scaled by the intensity inhomogeneity field  $b(\underline{x})$  so that the SNR is preserved [24].

$$s(\underline{x}) = (o(\underline{x}) + n_{bio}(\underline{x}))b(\underline{x}). \quad (3.4)$$

For images acquired in *low-field*, we can use, without loss of generality, the equation 3.3 for modeling the received signal. In this case, as we know that in the main part of the image  $n(\underline{x}) \ll o(\underline{x}) \cdot b(\underline{x})$ , we can achieve a good bias removal (as so that, image correction) by dividing the corrupted image  $s(\underline{x})$  by a correct estimation of the bias field  $\hat{b}(\underline{x})$ . So that, the corrected image can be expressed as:

$$\hat{o}(x) = \frac{s(\underline{x})}{\hat{b}(\underline{x})}. \quad (3.5)$$

So, if our approximation for the bias field is good enough to consider  $\hat{b}(\underline{x}) \cong b(\underline{x})$ , then we lead to the result:

$$\hat{o}(x) = o(\underline{x}) + \frac{n(\underline{x})}{\hat{b}(\underline{x})}. \quad (3.6)$$

In the parts of the image where  $n(\underline{x}) \sim o(\underline{x}) \cdot b(\underline{x})$ , the signal is not recoverable.

---

<sup>1</sup>We must recall at this point the FFT transformation presented in Chapter 2 for image computation (see equation 2.27)

The third MR image formation model is based in logarithmic transformed intensities, by which the multiplicative inhomogeneity becomes additive. We can see this last model as the logarithmic version of the multiplicative model. The signal modeled in this log-transformed intensities model can be written as:

$$\log(s(\underline{x})) = \log(o(\underline{x})) + \log(b(\underline{x})) + n(\underline{x}), \quad (3.7)$$

were the noise is still assumed to be Gaussian, which is methodologically convenient but inconsistent with the first model 3.27, where the noise is assumed to be Gaussian in the original non-logarithmic domain. Avoiding this fact, the corrected signal will be:

$$\log(\hat{o}(\underline{x})) = \log(s(\underline{x})) - \log(\hat{b}(\underline{x})) \cong \log(o(\underline{x})) + \frac{n(\underline{x})}{\hat{b}(\underline{x})}. \quad (3.8)$$

If we focus in the noise term of the corrected form, recalling it  $n'(\underline{x}) = \frac{n(\underline{x})}{b(\underline{x})}$ , we can see that the first factor ( $n(\underline{x})$ ) is a random term with zero mean and constant variance (in fact we are considering the noise as a Gaussian with zero mean). The second term,  $b(\underline{x})$  is a deterministic values which varies between 0 and 1 values. This fact lead us to have an strong dependence between the variance of the noise in the corrected image ( $n'(x)$ ) and the bias field value at the same point. That is, say that the noise variance is higher in the points where the bias value tends to zero. This behavior on the variance of the noise is due to the non-uniform Signal-to-Noise ratio along the data set of the acquired image.

## 3.2 Tissue Signal Distribution

The human brain is mainly composed by three different tissues: grey matter (GM), white matter (WM) and cerebrospinal fluid (CSF). Each of them has different concentration of water, and so, hydrogen atoms. This uneven number of hydrogen atoms in each element allows different excitations depending on the matter. This nucleous, present in water molecules, allow the soft-tissue contrast, specially with the MPRAGE acquisition protocol, giving different intensity values depending on the sort of tissue.

In fact, each MR image is modeled in the  $r$ -space (see eq.2.27) as a finite combination of regions. So for each type of tissue, we get a value of intensity that we model it. We assume this intensity distribution as Gaussian function of **mean**  $\mu_k$  and **variance**  $\sigma_k^2$  (see [4]), both are measured in gray levels and  $k$  identifies the different tissues . The probability of an intensity value in a voxel  $y_i$ , can be written (as long as be are assuming each pixel belong just to one class of matter) as:

$$P(y_i|\mu_k, \sigma_k^2) = \frac{1}{\sqrt{2\pi\sigma_k^2}} \exp\left(-\frac{(y_i - \mu_k)^2}{2\sigma_k^2}\right) \quad (3.9)$$

that means that for each type of matter in the brain we will have a gaussian intensity distribution fitting its brightness, so, in theory, we can to distinguish them. This model is useful for posterior processing techniques, like segmentation of tissues, where we identify the different tissues in the image for its treatment.

Unfortunately, the image not only presents noise, but also *Intensity Inhomogeneity (IIH or bias field)*. This artifact makes the intensity of a certain voxel shift from its mean value. If this shifting is big enough (and, unfortunately, it uses to be) the intensity value of the voxel can be considered to belong to the another class. In general, IIH artifacts makes the intensity of the pixel of the same tissue vary

significantly, overlapping with pixels of the different tissues.

For study this effects (the one due to the noise and the one due to the bias) we can compute the image histogram. The histogram of an image shows the relative frequency of occurrence of levels of gray in an image. That is,  $h(r_k) = \text{number of pixels with gray level } r_k$ .

Let us compare two different histograms:

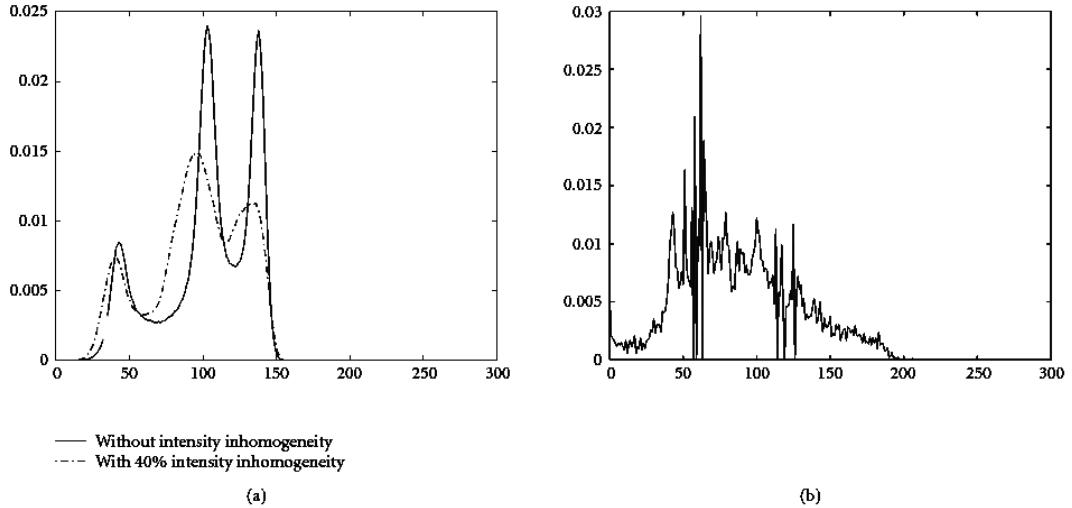


Figure 3.2: Histogram of brain tissue with IIH. Figure (a) shows two different histograms obtained from BrainWeb-simulated database page ([www.bic.mni.mcgill.ca/brainweb](http://www.bic.mni.mcgill.ca/brainweb)) one with noise and without IIH (solid line) and the other with noise and IIH (dashed line). Figure (b) is the histogram from a real brain image.

Figure 3.2(a) clarifies the bias field effects we want to explain. The tissue intensities had been modeled as Gaussian functions<sup>2</sup>(see eq. 3.9). So that, in Figure 3.2 we can distinguish the three tissues the brain is composed by. From left to right, the first peak represents the CSF matter, then we find GM and finally WM. When IIH is added to the simulation (dashed line on Figure 3.2), the differentiation becomes harder, as the IIH makes the amplitudes of the intensities of the tissues smaller and nearly similar. In fact, *noise makes the peaks get wider and IIH diminish its amplitude value*. This fact is which lead us to sometimes have wrong tissue classification.

### 3.3 The Noise in MRI

The noise, as seen before, is an important factor in our correction, so it will be useful to give a little insight on it.

The radio-frequency signals observed at the receiver (before they are FFT-transformed to give us a received signal), are corrupted by a noise that we assume

<sup>2</sup>Notice that we can do that because our intensity signal has noise (recall eq. 2.27) so it gives us some variance that allows us to model it as Gaussian.

to be thermal. This thermal noise is accurately modeled as *White and Gaussian-distributed noise*. Then, as the received signal, this noise is FFT-transformed onto the r-space (converting it from the k-space into spatial coordinates), but as the Fourier Transform is a linear transform, the noise distribution at the output, still remains Gaussian.

The problem appears after phase-encoding the signal<sup>3</sup>. Due to phase encoding errors, the reconstructed image will be complex, thus, there is white Gaussian noise on both real and imaginary components of the signal. That is, our noise becomes Rician if we take the absolute value of it [26].

The Rician *PDF(Probability Density Function)* is generated by taking the absolute value of two Gaussian random variables with non-zero mean. If we consider two deterministic measurements corrupted by additive Gaussian noise:

$$x_1 = \mu_1 + n_1, \quad (3.10)$$

and

$$x_2 = \mu_2 + n_2, \quad (3.11)$$

where  $n_1 \sim N(0, \sigma^2)$  and  $n_2 \sim N(0, \sigma^2)$ . Then  $x_1$  and  $x_2$  are both Gaussian random variables with  $x_1 \sim N(\mu_1, \sigma^2)$  and  $x_2 \sim N(\mu_2, \sigma^2)$ . Therefore, we can define a need random Rician variable as  $r = \sqrt{x_1^2 + x_2^2}$  with a PDF:

$$p_r(r) = \frac{r}{\sigma^2} \exp\left(-\frac{r^2 + A^2}{2\sigma^2}\right) I_0\left(\frac{Ar}{\sigma^2}\right), \text{ for } r > 0. \quad (3.12)$$

$I_0$  is the zeroth-order modified Bessel function for the first kind:

$$I_0(x) = \frac{1}{2\pi} \int_0^{2\pi} \exp(x \cos(\theta)) d\theta, \quad (3.13)$$

and  $A = \mu_1 + \mu_2$

The fact is that, actually, the noise associated with the acquired MR signal is generally taken to be additive, uncorrelated and Gaussian with zero (or low valued) mean [40]. So the signal can be modeled as:

$$s_m(\underline{k}) = s(\underline{k}) + \epsilon(\underline{k}), \quad (3.14)$$

where  $\epsilon(\underline{k})$  contains the sum over body and electronics contributions.

This assumption can be reached by understanding the noise influence in the spatial representation, considering that in the k-space the mean of the noise is zero:

$$\mu(p\Delta x) = \frac{1}{N} \sum_{p'} \overline{\epsilon(p'\Delta k)} \exp(j2\pi p'\Delta x \Delta k p) = 0, \quad (3.15)$$

and its variance:

$$\sigma_0^2(p\Delta x) = \frac{1}{N^2} \sum_{p'} \sum_{q'} \overline{\epsilon(p'\Delta k) \epsilon(q'\Delta k)} \exp(j2\pi p'\Delta x (p'\Delta k - q'\Delta k)), \quad (3.16)$$

---

<sup>3</sup>Phase-encoding, as we have seen in Chapter 2 (Section 2.3), is the proceeding for encode a 2D and 3D space in arbitrary coordinate

so it ends as:

$$\sigma_0^2(p\Delta x) = \frac{\sigma_m^2}{N^2} \sum_{p'} \sum_{q'} \delta_{p'q'} \exp(j2\pi p' \Delta x (p' \Delta k - q' \Delta k)) = \frac{\sigma_m^2}{N^2}. \quad (3.17)$$

We can extract as a conclusion from here, that we can assume the noise in MR acquisition is an additive single Gaussian distribution. That is to say, the noise is added to the factor obtained by multiplying the ideal images by the bias.

Regardless of whether the noise is Gaussian or Rician, high noise levels can significantly decrease the usability of medical imagery. The noise in the complex image can be viewed as continuous white Gaussian noise in four dimensions (three spatial and time) [6]. We might maximize the SNR by increasing acquisition time, increasing voxel size, increasing coil intensity and applying appropriate edge-preserving filtering techniques, carefully considering that all these methods have their limitations.

### 3.4 Bias Field in Low-Field Acquisitions

The MR bias problem occurs in all MR imaging applications. The extent with which it occurs and the amount of correction that is needed varies from application to application. *Intensity Inhomogeneities* (IIH) consist in an anatomically irrelevant variation throughout data generally reflected in a flip angle variation, but triggers in this variation can be multiple. Most tissues have some magnetic susceptibility which can distort the magnetic field; the main magnetic field  $B_0$  is not truly homogeneous in space, and the slope of the gradient-encoding  $B_1$  is not truly linear (see Chapter 2); the response of the transmitting coil (usually the body coil) is not completely uniform, and for the receiving coil, its response is not homogeneous either; the variations in  $B_0$  and  $B_1$  can produce location errors rather than intensity errors.

Those are some examples of the artifacts that can affect the image intensity in a MRI but there are some other that can have been grouped as follows:

- Artifacts related to acquisition technique.
  - Flip angle variation. One of the parameters set when acquiring the image is the **flip angle**<sup>4</sup>. One image is acquired forcing the hydrogen proton to turn in a certain angle and come back. This angle is the flip angle. The problem is that when increasing the field, this angle value loses homogeneity all over the brain as not all the spins rotate the same amount of degrees. This flip angle variation is one (let's us to say the main) cause of  $B_1$  inhomogeneities.
  - Non-uniform  $B_0$  static field. This inhomogeneity can be partially compensated by shim tuning. Its main effect is that leads to a partial deformation of the imaging plane.
  - Gradient fields. The variation in the gradient fields lead to geometrical distortions.
  - RF coil inhomogeneity which depends on its geometry and tuning. The inhomogeneity is seen in the transmitting coil as well as in the receiving one, but with different dependence with the  $B_1$  field.

---

<sup>4</sup>When talking about flip angle it refers to the flip angle of the macroscopic magnetization vector of the RF pulse.(see Chapter 2)

- MR acquisition pulse sequence parameters: repetition time, number of echoes, interleaved (or not) acquisition.
- Factors linked to the object itself. Tissue-dependent properties as conductivity and dielectric values. Besides, the acquisition protocol takes some minutes to be done, so the normal movements of the patient lead also to inhomogeneities in the acquired image too.

For a *Low-field acquisitions* (which means for main fields strengths lower than 3 Tesla), the bias field added to the image has been largely studied, so we have some good approaches for its form or value. In next Chapter we will present the State-of-the-Art of this bias correction methods and its drawbacks when correcting acquisitions at high fields.

### 3.5 Drawbacks when Increasing Field Strength

Nowadays, the bias field we obtain when acquiring a MRI is nearly assessed when the main field applied is not higher than  $3T$ . In fact, as we will see in Chapter 4.1 in the low field case, due to its slow and smooth variation, it can be approximate by some basis smooth functions, as the *Legendre Polynomials* so the approximation is good enough to be used to correct the original image from this artifact, even for the inhomogeneities induced by the patient. The complexity of the problem increases when increasing the field applied to the sample, as we start losing phase coherence so it appear dielectric effects and those due to the conductivity of the tissues. Those effects make the bias field act not as a smooth function, but as a **wave**.

As the field increases, the wavelength ( $\lambda$ ) of the field decreases, until the point of make the RF field comparable to, or even less than, the dimension of the human body. So, at high frequencies, the RF magnetic field (also called  $B_1$  field) inside a sample exhibits prominent **wave behavior**. But, how we can explain this behavior?

As the static strength ( $B_0$ ) increases, the frequency of the RF magnetic field (so  $B_1$ ) increases too and, so that, its wavelength decreases. The wavelength decreases even further in biological tissues, since many biological samples have high relative dielectric constants. Due to this decreasing, the wavelength and the sample size become comparable. And so, as the sample dimensions represents a larger percentage of a wavelength, **intermediate** and **far-fields effects**, including wave propagation, become more important. Actually, the significant interactions of the electromagnetic waves with the load invalidate the use of quasi-static approximations and require the application of the full wave techniques [32].

In brief, the **full-wave solution of Maxwell equations** demand is due to the presence of those *intermediate* and *far field effects* as the  $B_1$  effect that causes image inhomogeneity is wave interference [7]. In fact, when the applied main field is lower than  $3T$ , the far field approximation is good enough because the intermediate effects are small enough compared to the far-field ones, so the first ones are denied. But, increasing the main static field applied, those effects are no longer negligible.

Additionally,  $B_1$  field and source currents are strongly perturbed by sample loading. The high dielectric constant of tissue results in generating standing waves in the object that greatly perturb the effective  $B_1$  field. Due to electrical conductivity of the tissue, the induced voltage at high frequencies yield in eddy currents

large enough to attenuate the applied  $B_1$  with increasing depth in the body [14].

Besides, the  $B_1$  field distribution inside a sample is important for the Specific Absorption Rate (SAR). Specific absorption rate (SAR) is a measure of the maximum rate at which radio frequency (RF) energy is absorbed by the body when exposed to radio-frequency electromagnetic field. It is used for exposure to fields between  $100kHz$  and  $10GHz$  [1]. The SAR value will depend heavily on the geometry of the part of the body that is exposed to the RF energy, and on the exact location and geometry of the source of the RF energy. Actually, the electrical properties and size of the sample strongly affect the RF field distribution (in magnitude as well as polarization) at high field strengths.

The polarization of the RF field inside the sample varies drastically such that the RF field in certain regions can rotate predominantly in the direction opposite to the direction intended in driving the coil.

So, in resume, any mathematical approach of RF field inside the sample (and in our case, inside the brain) can be extremely complicated due to:

- The quasi-static approximations of Maxwell's equations are not valid. A full version of Maxwell's equations must be employed.
- Human body geometry is irregular and it has different conductivity and dielectric rates (specially in air-tissue boundaries).

Talking about brain imaging, non uniformity image intensity at high field is prominent and frequently observed when the human head images are acquired with a volume coil. It is reflected as a hyperintense region in the center of the head (see Fig. 5.1) and can be considered to be due to the partially-constructive superposition of RF waves transmitted from each of the conductors in the coil and reflected from the sample boundaries, plus the still-substantial near-field contributions. Artifacts due to wave behavior are initially observed at 3T and become more prominent in images acquired at higher field strength.

In resume, when imaging using MRI techniques, as frequency increases, electromagnetic waves decay faster in the brain (as human brain tissues are neither purely dielectric nor purely conductive) and the boundary between brain and air becomes less reflective. So that, the amplitude distribution of the fields in the head is the result of the interference pattern of decaying traveling magnetic waves in a given sample-coil configuration plus contribution from near fields. Besides, and no less important, electromagnetic properties of grey and white matter for human brains are inverse: conductivity increases while dielectric constant decreases with frequency, which means that the bias field is different in both.

Arguably, the major problem of these 7T images acquisitions is that we can not make the assumption that the bias has a smooth variation anymore. And this, unfortunately, is almost the only supposition used in almost all kinds of *retrospective* methods for bias correction and/or compensation in human brain imaging.<sup>5</sup>

---

<sup>5</sup>Retrospective methods are postprocessing methods that propose to correct MR images with only few assumptions on the acquisition process. In Chapter 4.1 we will make an overview of some of those methods.

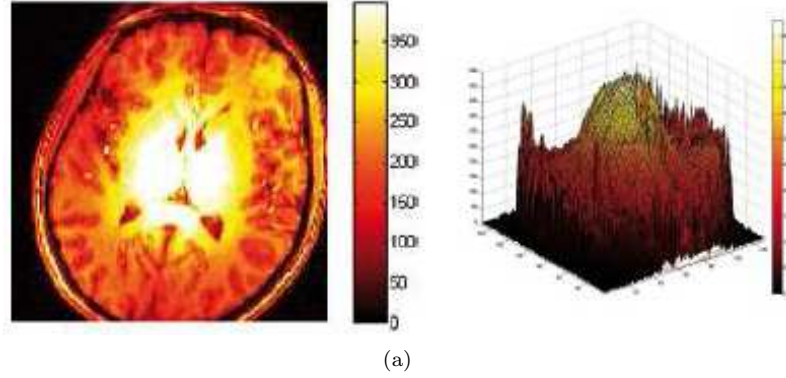


Figure 3.3: Hyper-intense region in the center of the head at 7T and its 3D view .

### 3.6 Bias Field in High-Field Acquisitions

As seen above, RF behavior becomes complex at ultra-high magnetic fields. A bright center and weak periphery are observed in images obtained with volume coils. Destructive interferences are responsible for this variations of brightness in the image [37]. But, how we can model the signal intensity in such acquisitions?

In paper [16] a study for the polarization of  $B_1$  field over a water phantom is performed. It would give us an insight of wave behavior we want to model in 7T acquisitions. Following its wave behavior and after considering full-solution Maxwell equations, the transmitted field can be decompose into two rotating components:

$$\begin{aligned}\hat{B}_t^+ &= \frac{(B_{tx} + iB_{ty})}{2} \\ \hat{B}_t^- &= \frac{(B_{tx}^* - iB_{ty}^*)}{2}.\end{aligned}\quad (3.18)$$

Where the absolute value of the polarization component  $|B_t^+|$  is given by:

$$|B_t^+| = ([Re(B_t^+)]^2 + [Im(B_t^+)]^2)^{\frac{1}{2}}.\quad (3.19)$$

The calculation for the receiving field is similar. The reception field  $B_r$  can also be decomposed in two circularly components:

$$\hat{B}_r^+ = \frac{(B_{rx} + iB_{ry})}{2}\quad (3.20)$$

$$\hat{B}_r^- = \frac{(B_{rx}^* - iB_{ry}^*)}{2}.\quad (3.21)$$

where

$$|B_r^+| = ([Re(B_r^-)]^2 + [Im(B_r^-)]^2)^{\frac{1}{2}}.\quad (3.22)$$

The transmission and reception fields are two physically different fields, so they must be calculated separately for producing the image intensity distributions. Actually, the polarization behavior of RF field plays an important part in the formation of the image intensity distribution in a human sample at high field. The transmission field is produced by the input current in the coil and the reception one by the current induced by the transverse magnetization. This leads the transmission field

rotate in the same direction as the magnetization precession whereas the reception field rotates in the opposite direction. The later one is used when the principle of reciprocity is applied for evaluation of the reception distribution.

In figure 3.4(a), the plot for  $|\hat{B}_t|$  shows the field strength distribution, while  $|\hat{B}_t^+|$  and  $|\hat{B}_t^-|$  depict the positive and negative circularly polarized components of the transmission field. The  $\beta_t$  contour plot (shown in figure 3.4(b)) describes the polarization distribution of RF field without the implication of the spatial field strength variation.<sup>6</sup> [37].

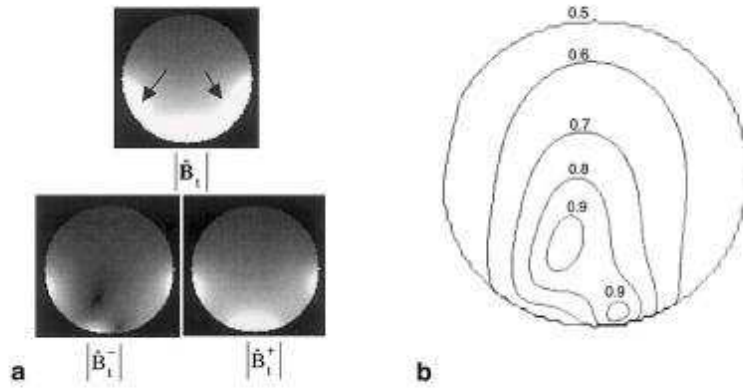


Figure 3.4: Grayscale plots of the transmission field and its circularly polarized components (a), and the contour plot of  $\beta_t$  (b) of the quadrature surface coil in free space ( $\sigma = 0$ ,  $\epsilon_r = 1$ ). This plot is a ratio of the transmission field defined as  $\beta_t \equiv \frac{|B_t^+|}{|B_t^+| + |B_t^-|}$  Image obtained from paper [16]

The overall intensity of  $|B_t^+|$  is significantly stronger than  $|B_t^-|$ , whereas  $|B_r^-|$  is much stronger than  $|B_r^+|$ . So, from here, we can assess that the direct responsible for the MR image intensity distribution are on one hand  $B_1$  field, and on the other hand its circularly (actually elliptical) polarized components  $B_t^+$  and  $B_r^-$ . So, from this moment, we will consider  $B_1^+ = B_t^+$  and  $B_1^- = B_r^-$ .

In resume, the RF field interacts with magnetization through the circularly polarized components, which can be constructed on an axial plane through the center of the sample as:

$$\begin{aligned} \hat{B}_1^+ &= \frac{(B_x + iB_y)}{2} \\ \hat{B}_1^- &= \frac{(B_x - iB_y)}{2}, \end{aligned} \quad (3.23)$$

assuming that  $\hat{B}_1^+$  is in the direction of nuclear precession, so that, is the component that determines the excitation.

<sup>6</sup>The nuclear spin precession is assumed to be in the positive (counterclockwise) direction.

In the **low field** case, the  $B_1$  and its circularly polarized components  $\hat{B}_1^+$  and  $\hat{B}_1^-$  can be considered real factors, so the spatial distributions  $|\hat{B}_1|$ ,  $|\hat{B}_1^+|$  and  $|\hat{B}_1^-|$  are essentially the same. Arguably, in this quasi-static regime the difference in the relative spatial distribution between the  $B_1$  field magnitude and its polarization components is insignificant. The magnitude of the transverse  $B_1$  can be directly used to assess the signal intensity distribution.

However, at 7T, as the wavelength of this field approximates the size of the human brain sample, the distributions of the transverse field magnitude and its circularly polarized components are markedly different and only the latter can be used to represent signal intensity.

In fact, in presence of wave behavior at **high fields**, the distributions of these quantities are significantly different. In this case  $|\hat{B}_1^-|$  must be used to calculate the contribution to the image intensity.

The image intensity distribution  $I$  due to excitation (transmission) is:

$$I \propto \rho \sin(V|\hat{B}_1^+|\gamma\tau), \quad (3.24)$$

with  $\gamma$  the gyromagnetic ratio,  $\tau$  the excitation pulse duration and  $\rho$  the spin density.  $V$  is a dimensionless factor, proportional to the coils driving voltage and thus proportional to the flip angle. Whereas, for reception,  $I$  is proportional to the RF field generated by the coil according to the reciprocity principle. Hence:

$$I \propto \rho V|\hat{B}_1^+|\gamma\tau, \quad (3.25)$$

Thus, in this case the image intensity can be calculated by <sup>7</sup>:

$$I \propto \rho \sin(V|\hat{B}_1^+|\gamma\tau)|(\hat{B}_1^-)^*|. \quad (3.26)$$

As the equation 3.26 shows, the image intensity depends sinusoidally on  $|\hat{B}_1^+|$ , which is the dependence with the transmitted field and linearly on  $|(\hat{B}_1^-)^*|$  (which is the received one) [16]. This difference in excitation and reception leads to an asymmetric image intensity distribution. In fact, if the *flip angle is small* (which happens in the FLASH acquisitions but not exactly in the MPRAGE ones), the global signal intensity is approximately proportional to  $|\hat{B}_t^+| \times |B_r^-^*|$ . <sup>8</sup>

Moreover, wave behavior of the RF field makes not only change the intensity distribution in the image. Other values present distortions due to the bias field as they are also RF dependent. SAR and SNR also present problems at higher fields. The increase of SAR (see Section 3.5) may be *linearly proportional to  $B_0$  in the center of the brain to quadratically proportionally in the brain periphery* with a homogeneous RF coil [38]. This  $B_1$  field enhancement in this center region of the brain (which appears as a bright spot) is due to the dielectric volume resonance effect related to the object size and the wavelength of the RF pulse [14]. Similarly, the signal-to-noise ratio (SNR) is also dependent on the  $B_1$  contour as well as  $B_0$ , increasing a

<sup>7</sup>It is important to notice that when talking about signal intensity we actually refers to the signal obtained after the Fast Fourier Transformation from the  $k$ -space to the  $r$ -space. That is, we mean the signal obtained when applying equation 2.27. From this point, and for facilitate the notation, we will call  $s(\underline{x})$  as  $I$  or  $SI$ .

<sup>8</sup>We must be careful with this assumption: this approximation is no longer valid when we cannot assume a small flip angle approximation, due to an increment on transmission power or stronger transmission field in certain areas.

better than linear proportion in the brain center and at less than linear rate in the brain periphery when a homogeneous coil is used. In brief, SAR and SNR as well as image inhomogeneity and contrast vary with the  $B_1$  contours in the anatomy [38].

### 3.7 Summary of Analysis of Bias Field

In this chapter we have presented an approximation for the bias field in MR acquisitions, and for the noise added in the images. This approximation is needed in order to find methods to compensate it and give a clear image of the tissues we want to study.

The general model for the signal intensity presuppose, without loss of generality, an multiplicative bias field and an additive white gaussian noise. That is:

$$s(\underline{x}) = o(\underline{x})b(\underline{x}) + n_{RM}(\underline{x}). \quad (3.27)$$

For **low-fields acquisitions** (which includes the acquisitions performed with fields lower than  $3T$ ), the *IIIH* manifest itself as a smooth spatially variation and it has been modeled by fitting its shape with *smooth functions*. Otherwise, we have seen that when increasing the main field value, this assumption is no longer feasible.

For **high-field acquisition**, the bias field acts as a standing wave so the full-wave solution of Maxwell equations is needed. As frequency increases, the wavelength decays faster and the boundaries between tissues become less reflective and this leads on contrast lost between tissues. The amplitude distribution of the magnetic field is the result of the interference pattern of decaying traveling waves plus the contribution of near-field effects.

So that, any mathematical approach of the RF field inside the sample can be complicate. The methods for bias compensation in this case must take into account other factors, as we will see in next Chapters.

The main contribution of this master thesis is demonstrate that, due to this wave behavior, the bias field corrections performed until now are not enough for correcting  $7T$  acquisitions. All the conclusions and results we will shown in posterior Chapters are based in the fact that at  $7T$  the bias can not be assumed as a slow and smooth variation. This report focus in MRI acquisition of human brains images, but actually, the bias appears in all MR imaging techniques, whereas we are imaging the brain or other parts of the body. So that, the conclusion we will assess for the specific case of the brain, can be extrapolate to other MR images.

## Chapter 4

# State-of-the-Art Methods for Bias Correction

Since the apparition of the MR techniques for imaging human body, automated analysis had become mandatory to efficiently cope with the large amount of data generated using them. Besides, several artifacts affect the quality of the data, with a considerable amount of degradation. Huge efforts had been placed on finding methods to erase (or at least compensate) the bias field from the image. In fact, the goal of all this methods is to facilitate all the quantitative and qualitative analysis of this data, like segmentation or registration protocols.

This Chapter is an overview of the most important methods proposed in the recent literature. We will enumerate some of them and, after that, we will focus on specific ones, validating them for our specific purpose: bias correction in  $7T$  acquisitions.

### 4.1 Prospective and Retrospective Methods

Intensity non uniformity (INH) has different sources. Actually, such artifact that can affect the image intensity can be related (1) to the *acquisition technique*, as they can be induced by the coils used in the acquisition protocol, the sequence selected or related to (2) the *nature and the geometry of the sample*, as RF penetration or RF standing wave effects, otherwise [5]. Considering this rough division, we can assume two different parts in the MRI correction process, sorting all the existing methods according their location in the acquisition/processing pipeline and on the assumptions those methods rely on. We can define:

- **Prospective methods**, focused on the **acquisition part** which is, let us to say, the "physics" part.
- **Retrospective methods**, that rely on the **post-processing part**, so we can consider them to belong to the signal processing methods.

For the first ones, their goal is to improve the acquired image quality by a better acquisition protocol. Image processing community, instead, try to improve this quality by the use of retrospective algorithms as first steps to improve quantitative analysis. This is a rough classification of the correction/compensation methods for bias in MR acquisitions, as most of them rely in different assumptions.

### 4.1.1 Prospective Methods

Prospective methods are based on prior knowledge about acquisitions parameters. If we recall the signal model seen in Chapter 2 (equation 3.3)

$$s(\underline{x}) = o(\underline{x})b(\underline{x}) + n_{RM}(\underline{x}), \quad (4.1)$$

we notice we have an ill-posed problem: neither the bias,  $b(\underline{x})$ , nor the true intensity spatial distribution,  $o(\underline{x})$ , are known. But, we can get a prior knowledge of them by using specially designed MR acquisition protocol.

These methods suppose the IIIH due to the combined effect of (1) the sample, (2) the MR pulse sequence and (3) the coils, so to get knowledge of one (or more) of this parameters can facilitate the way for bias correction. That is, prospective methods try to *reduce the number of unknown factors involved*. We can find two main different approaches to this purpose:

1. Combine different data sets.
2. Trying to compensate unwanted flip angle variation during the acquisition process.

#### Different data sets combination

There are several ways to get multiple data set combinations. One first approach is to acquire images from different objects (usually phantoms) with the same imaging parameters [5]. In this case we will be considering data sets only affected by sequence-dependent and coil-dependent components of IIIH. So, once the parameters are set, *the IIIH will be directly related to the coil sensitivity*. This gives a good representation of the receiving coil sensitivity variation [3]. The main limitation is that this approach does not take into account the influence of the imaged object. And as we have seen in Section 2.6, this effects can be really important when increasing the main field strength. So that, those methods are not valid for bias correction at 7T MR imaging.

Other methods face the problem from another point of view: they acquire data sets of the same object changing the imaging parameters. In this case, they try to *remove the IIIH component due to the object studied*. In fact, they get a priori knowledge of the bias field added by using different acquisition protocols or different coils [5].

Liney et al., in 1998 [22], use same coil acquisitions with different imaging parameters, considering that an homogeneous tissue is modeled by an homogeneous intensity distribution (see Chapter 3.1, section 3.2, equation 3.9)

$$P(y_i|\mu_k, \sigma_k^2) = \frac{1}{\sqrt{2\pi\sigma_k^2}} \exp\left(-\frac{(y_i - \mu_k)^2}{2\sigma_k^2}\right). \quad (4.2)$$

In this case, any variation in signal intensity is attributed to the bias field. So, they consider the corrupted data as a representation of the bias field spatial variation. They assessed that a *T2-weighted sequence* can be corrected using the bias estimation obtained from a *PD-weighted (proton density)* sequence.

In all this cases, the correction is not complete, as they are only focusing in one of the sources of the bias. In low-field case, the bias is not as strong as the one we get when working at high-fields strengths. Is for that reason, that those

methods, even if they just focus in one origin of the IHH, work in a acceptable way in low-field acquisitions but not as good as we want in high-fields. So, and without denying them, we can assess that those prospective methods are not suitable for our purpose: bias correction in  $7T$  acquisitions.

Instead of acquiring different set using the same coil but changing image parameters, we can fix this parameters and acquire the data set changing the reception and transmission coils. Surface coils have good SNR but really poor uniformity, while body/volume coils are assumed to have uniform sensitivity. A pre-scan of localization data can also be performed, to obtain prior knowledge about the bias field.

### **Flip angle variations compensation**

A part of the multiple set combination, prospective methods with *pre-acquisition flip angle compensation* had been performed too. Actually, as we will see in Chapter ??, *in this master thesis we propose a method which combine the acquisition of a flip angle map with some post-processing techniques applied to the acquired image to perform its correction.*

Coming back to our topic, this second group of prospective methods, assume the IHH mainly due to the RF coil, so they first estimate the sensitivity for a particular head coil along the  $z$  axis. Then they compute a *Look-up-table (LUT)* to correct the variations based on the estimate sensitivity profile [8].

Deichmann et al., in [11] designed an specific RF excitation pulse, based on two spatially independent terms, compensating unwanted flip angle variations in a head coil. Actually, this master thesis will give lay in this method, giving a different approach from the one assess by Deichmann (that will be in Chapter ??). We will propose (see Chapter ??) the use of a flip angle map (also called RF map or  $B_1$  map) for determine the bias in the acquisition. In that way, and using post-processing methods (id est, a retrospective method), we will try to correct the bias in the MR acquisition.

*In fact, the main goal of this thesis is to give a bridge between the prospective methods and the retrospective ones. Instead of focusing in compensate the bias field acting only in one of the, let's say, segments of the acquisition/processing protocol, we will try to combine techniques applied in both of them.*

The main idea is that we can combine the knowledge obtained from both segments. That is, if the methods proposed at this moment are not god enough for achieving the correction, why don't combine two of them, to get better results?

### **4.1.2 Retrospective Methods**

Retrospective methods propose to correct MR images corrected by IHH artifact with only few assumptions regarding the acquisition process. We will focus on them as, from the point of view of signal processing, they are capable to compensate the bias in a more generic way than the prospective methods do.

They can be classified in *grayscale level-based* or *transform domain based* methods.

## Grayscale Level Based Algorithms

The grayscale level based algorithms rely on the assumption that the bias has smooth spatially and slow varying across the image, so the ideal image becomes piecewise constant [5]. Different approaches had been mainly developed, focusing either on assumption concerning the artefact or the true image:

**Surface fitting:** Is a type of interpolation. Its aim is to *fit a set of data points* to provide a good approximation of the brightness function of the image. Correction is performed dividing voxel-by-voxel the original image by the computed surfaces following the principle shown in Chapter 3.1, in equation 3.6. Depending on the type of the basis function used, we can find different solutions.

*Polynomial Basis Functions:* Styner et al., in [31], propose a *Parametric Bias Correction* for MR images. It is a multiple pass basis function fitting. Considering the assumption of smooth and low variation of the bias, they estimate it by Legendre Polynomial, computing its coefficients by minimizing an energy function. In section 5.1 we will talk about it in a broad way.

*Spline Basis Functions:* Those methods fit the basis function by single pass fitting or multiple pass fitting.

**Spatial filtering:** The main assumption of this methods is that the bias is a *low spatial frequency intensity variation*. So, the methods based in spatial filtering, first extract the IHH, and then perform the correction by dividing the original image by the extracted IHH. This spatial filtering is has been generally done with two different kind of filters: the *Low-Pass filter* and the *Homomorphic filter*.

*Low-pass filtering* techniques are normally based on Median filter as it is useful for removing outliers (extreme pixels/voxels values). It uses *sliding-neighborhoods*, ordering the pixel/voxel values in a neighborhood prior to choose the median value as a result.

*Homomorphic filtering* is a non-linear filtering technique for image enhancement or correction. This filtering methods rely on the fact that The Fourier transform is linear and associative under addition, but is not associative under multiplication. Thus, Fourier methods are suitable for removing noise from images only when the noise can be modeled as an additive term to the original image. In general image signal processing, when the noise is not additive, we can define an object in terms of the illuminance and reflectance so, an image of the object might be modeled as  $f(x, y) = i(x, y)r(x, y)$ . According to this approach, input signal is assumed to consist of two multiplicative components: background and details. Illumination and reflectance are not separable, but their approximate locations in the frequency domain may be located. Illumination variations can be thought of as a multiplicative noise, and can be reduced by filtering in the log domain. To make the illumination of an image more even, the high-frequency components are increased and low-frequency components are decreased.

If we consider equation 3.27, we realize that for an MR image, the bias ( $b(\underline{x})$ ), which is the artifact we want to remove, multiplies our 'ideal image' ( $o(\underline{x})$ ), so is direct to identify "reflectance" and "illumination" as "image" and "bias". So, ideally, Homomorphic filtering is supposed to diminish the bias contribution in the image.

**Statistical methods:** Those methods mainly aim at segmentation, but they

take IIIH into account as it is an important factor that can distort segmentation results. It can be achieved by means of *Maximum-Likelihood (ML)* and *Maximum-a-Posteriori Methods (MAP)*-based methods or by *Fuzzy-C-Means*-based methods. The first two, label pixels according to probability values, which are determined based on the intensity distribution of the image. It is an estimation problem that can be based in different criteria as MAP or ML. Parameters estimation can be achieved by *EM (Expectation-Maximization)* algorithm. The expectation step is equivalent to compute the posterior tissue class probability (see. Section 3.2) when the bias field is known while the maximization step is equivalent to a MAP estimator [5].

The *Fuzzy-C-Means*-based methods clusters data by computing a measure membership, called the fuzzy membership, at each voxel for specified number of classes. However, FCM is not appropriate for data corrupted by IIIH [5].

### Transformed Domain Based Methods

All the graylevel-based methods work in the spatial domain, but they also work in other domains as the Fourier or wavelet domain (which are dual), or in the complementary domain of probability density functions (PDF). Some methods had made this change of domain, as they can make different assumption on the bias.

When computing the PDF, the original intensity spatial distribution becomes *intensity probability distribution* that we can model as an histogram. In this case the IIIH is considered as a parasitic convolution term which increase entropy. The idea of those methods is to minimize this entropy and deconvolute the parasitic term to correct the image [39].

Working on *Fourier Transform domain* has been seldom used in IIIH correction. In fact, normally, the filtering is done in spatial domain (as we have seen in the previous subsection).

Recently, the used of *Discrete Wavelet Transform* have been proposed. In [21], Lin et al., use the DWT to decompose the image into a cascade of orthogonal approximation and detail subspaces for different spatial resolutions. Each approximate subspace contains low-frequency information whereas the corresponding detail subspace contains high-frequency information. the information of those to subspaces can be combined to achieve IIIH correction.

## 4.2 Summary of State-of-the-Art Methods for Bias Correction

Since the apparition of the MR imaging techniques, the main goal has been to achieve good soft tissue imaging, developing methods to enhance contrast and resolution. In this Chapter we have presented a resume of the State-of-the-Art methods for this achievement, methods for bias correction

We cannot forget that MR imaging techniques are in constant development. MR has always been moving to ever higher magnetic field strength. In point of fact, increasing the main field strength allow us to get advantage of a better **signal-to-noise ratio** (which increases almost linearly with the field strength [27]). This improvement of the **SNR** allows higher spatial resolution and/or faster imaging,

a greater spectral dispersion, as well as an enhanced sensitivity to magnetic susceptibility. But, if we increase the field, we find unsuitable effects or artifacts that cannot be treated as we have been doing with low-field acquisitions. And this fact becomes a problem.

Actually, all these methods are plenty proved in low field acquisitions. They are *based in the assumption of smooth and slow variation of the bias field along the image*. Unfortunately, as we have seen in Chapter 3.1, for high field strengths these assumptions are no longer correct. That means, the methods are no longer suitable for our purpose: bias correction in 7T MRI acquisitions. In next Chapter we will present some studies about two of the grayscale based methods, showing its drawbacks in the correction at high fields. The *PABIC (Parametric Bias Correctic)* and the *LPF (low-pass filtering)* approaches are studied, and analyzed. In Chapter ??, a new method is presented, a method which try to palliate this deficiencies.

## Chapter 5

# Analysis of Retrospective Methods

In the Chapter 4, we have presented the State-of-the-Art methods used nowadays for bias correction, sorting them in two different categories: prospective and retrospective methods. The idea is to show that, even though those methods have been largely tested in low-field MR acquisitions, they become weak for correct images acquired at higher fields. That is, the main drawback of these methods appears when we increase the main field strength as they have not demonstrated to be able to correct the image IIH due to RF field inhomogeneities.

In this Chapter we will study the two mainly used methods for correction of MR images, proving its unsuitability for achieving IIH correction in MR acquisition of over  $7T$ . The PABIC and the Low-Pass filtering approaches are studied. Our goal is to achieve a common brightness level for each tissue in the image. The quantitative analysis will be performed in terms of the **Mean Square Error (MSE)** between the corrected image and the image assumed as Ground Truth and the **time elapsed** in the simulations. Notice that the power of the computer is responsible for the time elapsed when running the correction. The tests had been performed over an Intel(R) Core(TM)Duo CPU 6600 @2.40GHz, 1.98GB of RAM.

We should clarify that, when talking about  $7T$  MR acquisitions, it is difficult to assess the quality of the correction as we only deal with corrupted data, so even the ground truth used for the comparison presents some bias corruption.

### 5.1 The Parametric Bias Correction (PABIC)

As seen before, the PABIC is a retrospective method for IIH correction mainly developed by Martin Styner from the University of North Carolina. This polynomial approach combines bias correction with histogram adjustment. It is not only focused on bias correction. In fact, besides the correction of intensity inhomogeneities in magnetic resonance imaging (MRI) it significantly improves intensity-based tissue segmentation. Actually, at the same time as the bias correction, and to facilitate it, PABIC runs a tissue segmentation of the image, with the estimation of mean and variance values assessed for each tissue by the user.

PABIC is based on a simplified model of the imaging process: a parametric model of tissue class statistics, and a polynomial model of the inhomogeneity field. The authors [31] assume that the image is composed of pixels assigned to a small

number of categories with a priori known statistics. Further they assume that the image is corrupted by **noise** and a **low-frequency inhomogeneity field**. The estimation of the parametric bias field is formulated as a nonlinear energy minimization problem using an evolution strategy (ES). The resulting bias field is independent of the image region configurations and thus overcomes limitations of methods based on homomorphic filtering. Furthermore, PABIC can correct bias distortions much larger than the image contrast.

The main idea of this method is to determine the correct class  $k$  which each pixel/voxel belongs to, in order to obtain an intensity-based segmentation of the image. As we have presented in Chapter 3.1, human brain have three main classes of tissues: white matter (WM), gray matter (GM) and cerebrospinal fluid (CSF), thus, in this case,  $k = (1, 2, 3)$ . Here, we must make a consideration. Human brain, a part from this three types of matter, is composed by other classes such as skull, skin, blood vessels... This classes are considered to be too small and morphologically complex to help in the correction so, in a previous step, they are removed by pre-processing protocols as *skull-stripping* and *masking*. We will talk about them later.

The Parametric Bias Field Correction (PABIC) relies, in one hand, on the model of the image intensity presented in Section 3.2 and, in the other, on the fact that  $b(\underline{x})$  can be thought as a combination of  $m$  smooth basis functions (which are *Legendre Polynomials*). In this method,  $b(\underline{x})$  is modeled as  $b'(\underline{x}, \underline{p})$ , where  $\underline{x}$  are the spatial coordinates and  $\underline{p}$  the coefficients of the Legendre Polynomials.

The  $\underline{p}$  parameters are estimate directly from data by the iteratively search of the global minimum of a energy function, stepping-out from non-optimal minimum [31]. This energy function is:

$$e(\underline{p}) = \sum_i (u_i - v_i(\underline{p}))^2, \quad (5.1)$$

where  $u_i$  is the data and  $v_i(\underline{p})$  is model a used to parameterize single-class model and is found between Valley functions which is a robust family of M-estimators:

$$valley(d) = \frac{d}{d^2 + 3\sigma^2}, \quad (5.2)$$

showing inflection points at  $d \pm \sigma$ . The valley functions of each class are multiplied so the total energy function remains:

$$e_{totimage}(\underline{p}) = \sum_{\underline{x} \in image} \Pi_k valley(s(\underline{x}) - \hat{b}(\underline{x}, \underline{p}) - \mu_k). \quad (5.3)$$

We must know that finding  $p(\underline{x})$  by minimizing this energy function is a nonlinear problem. The method used in PABIC for this minimization is the *1+1ES algorithm*, where each  $p(\underline{x})$  represent an individual. Its operation is shown in Appendix E.

PABIC rely in some assumptions:

- The bias field ( $b(\underline{x})$ ) has slow and smooth variation and its mainly due to the RF field and partially induced by the patient.
- The bias field ( $b(\underline{x})$ ) can be approximate by a parametric model  $\hat{b}(\underline{x}, \underline{p})$  as a superposition of Legendre Polynomials.
- The intensity of the signal for a given class is modeled as a Gaussian of mean  $\mu_k$  and variance  $\sigma_k^2$ .

- The hypothetical idealized signal ( $o(\underline{x})$ ) consists on pixels/voxels  $\underline{x}$  each of which can be assigned to a unique tissue class.
- Noise ( $n(x)$ ) is caused by biological tissues.

This method is fully automatized, and prior to its application to a specific image some parameters must be set. This parameters are divided in three groups: (1) parameters for the class model, (2) parameters for the bias field model and (3) parameters modeling the optimization. They are listed below:

1. Class parameters:
  - Number of classes
  - Mean and variance values for each class
  - Class mask
2. Bias estimation parameters:
  - Type of bias field
  - Order of Legendre Polynomials
3. Optimization parameters:
  - Mutation factors  $c_{grow}$  and  $c_{shrink}$
  - Maximum number of iterations
  - Initial values of coefficients  $p$

## 5.2 Results and validation of PABIC Method

To test PABIC reliability in bias correction over  $7T$  acquisitions, several test over an MPRAGE acquisition had been performed, treating the PABIC algorithm as a "black box". We have used the utility *MRI Bias Correction*, developed by Martin Styner, from the *ITK C++ library* [15]. ITK is a cross-platform application development framework, widely used for the development of image segmentation and image registration programs. ITK was developed with funding from the National Library of Medicine (U.S.) as an open resource of algorithms for analyzing the images of the Visible Human Project. ITK stands for The Insight Segmentation and Registration Toolkit. The toolkit provides leading-edge segmentation and registration algorithms in two, three, and more dimensions.

As said in the previous section, some parameters must be set before running *Bias Correction* utility. The *class parameters* must be set, as well as *bias estimation parameters*. *Optimization parameters* are not compulsory, so in this first attempt we denied them, working with the default ones.

The choice of the mean and the variance values of each class is not trivial. In fact, PABIC set values for those variables are mainly used to distinguish between the different tissues in the segmentation process which is done parallel to the bias correction. Thus, it is important to assess them in the most accurate way, to avoid wrong results in the process. For this purpose, we compute the histogram of the test image and try to accurately discern all the classes considering the peaks in the histogram.

The first tests were performed with a single slice of an high contrast acquisition of a human brain at  $7T$  (see Fig.5.1)

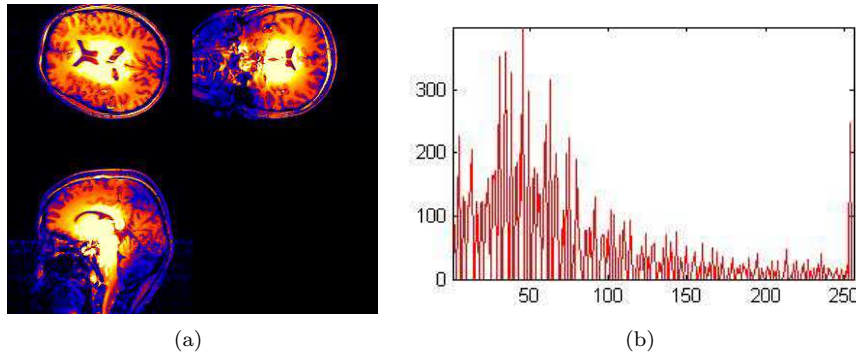


Figure 5.1: 2D human brain image used for first test in bias correction with PABIC. Single slice for a 7T MPRAGE acquisition corrupted by noise and bias (a) and plot of the computed histogram of its axial view (b).

In order to improve the results, we mask the image. This lead us to avoid the parts of the image that are not useful for bias estimation, such as the background. In fact, removing the background allow us to get better results even in computation time, as we are dealing with less information. Both, original and mask images must have the same size. The mask will be superposed over the original image, determining the pixels of this image that will be dismissed. PABIC can also use a default mask (in case the user does not introduce its own costumed mask). This default mask is automatically computed by setting to zero value the pixels which gray level is bellow the 10 per cent of the histogram.

Masking is normally the first step performed in almost all the image processing protocols. Its utility is to separate the useful data from the noisy background, removing this last one. It lays on the hypothesis that the background is the darkness part of the image, and so that, with the lower gray value in our scale<sup>1</sup>. So that, the simplest way to compute a mask is by simply threshold the graylevel values in the image, denying the pixel whom value is smaller than this threshold. There, we will have a binary image<sup>2</sup> so we can multiply it with our image and take only the values inside the mask. Figure 5.2 shows the mask used for correcting a 2D slice:

### 5.2.1 Correcting a 2D Human Brain Image

For testing the goodness of PABIC some features are used. We used the *p-vector* and the *time elapsed* in the simulations. Remember that each p-vector can be represented in a *m*-dimensional Euclidean space, so we use this output to compare different simulation, taking advantage of some Euclidean operators such as the distance between them and the ground-truth.

The first test performed, was to run consecutive simulations of the same data with the same conditions but changing the variance of the filter before the masking<sup>3</sup>.

<sup>1</sup>Actually, images in standard formats are stored so that each pixel/voxel value lies in a range [0..255]. This range is chosen so that each pixel/voxel can be represented by 8 bits (one byte). So, in this scale, 0 stands for black, 128 for gray and 255 will represent white.

<sup>2</sup>Binary image is an special kind of intensity image. Contains only 2 levels, 0 for black and 1 for white.

<sup>3</sup>In fact, before masking the image, is usual to low-pass filter it to erase part of the noise. In this case, the filtering had been done by changing the variance of the filter, with a fixed window

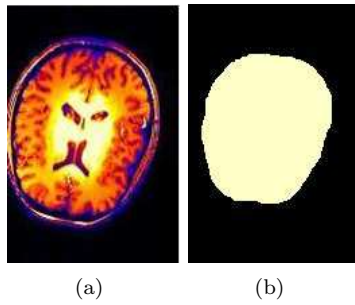


Figure 5.2: 2D human brain image used for first test in bias correction with PABIC. Single slice for a 7T MPRAGE acquisition corrupted by noise and bias (a) and the mask used for avoiding background (b).

We set the parameters of PABIC as follows: grade  $m = 3$  for Legendre polynomials and maximum number of iterations 200000 with a personal mask. For this case, we took as class-means the values  $\mu_1 = 129$  and  $\mu_2 = 198$ . And for the class-sigma,  $\sigma_1 = 22$  and  $\sigma_2 = 12$ . In figure 5.3, the evolution of the computing time is represented.

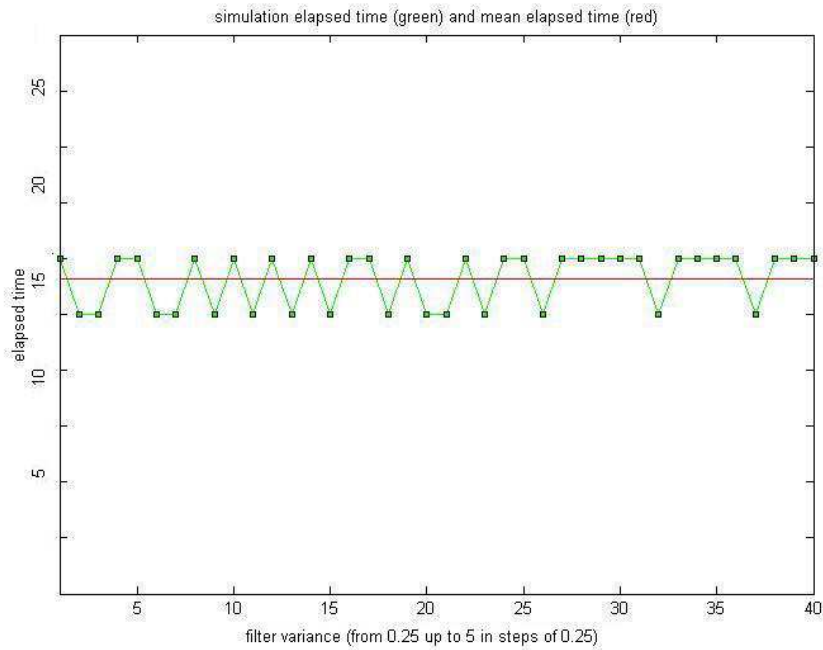


Figure 5.3: Evolution of the elapsed time in simulation while changing pre-filter variance

As we see in the image, the mean time elapsed is about 14 minutes. This time is not extremely big, otherwise the correction performed by PABIC is not good. In fact, if we take a look to the correction and its vertical and horizontal profiles, we realized the are not enough homogeneous, that is to say, the intensity is not uniform along the brain (see Figure 5.4). As an additional point, notice that the vertical profile has a greater slope than the horizontal one. This is because the vertical section is

size

parallel to the surface coil direction<sup>4</sup>

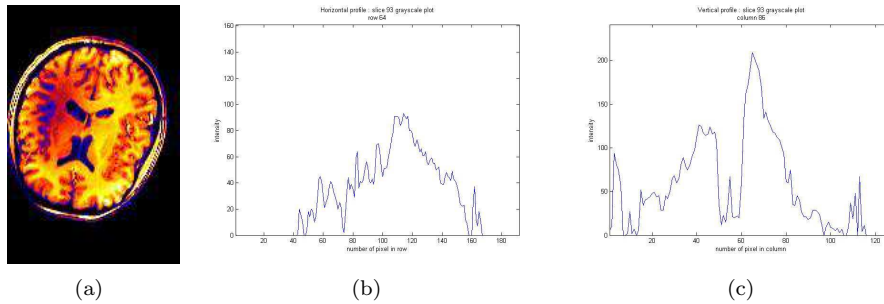


Figure 5.4: 2D human brain image corrected with PABIC (a) and its grayscale profiles. Horizontal profile (b) and vertical profile (c).

Due to the bad results obtained in our first test, a second experiment was performed. In this case, we tried to improve the correction of a 2D acquisition by changing the value of the maximum number of iterations allowed. In this case, we run PABIC with the same mean and variance parameters, and with  $m = 3$  as the degree of the Legendre polynomials. Here, a computation of the evolution of the *Mean Square Error* between the  $p$ -vectors was performed. For this purpose we averaged all the  $p$ -vectors obtained after the simulation get stable. The modulus of our averaged vector (our ground-truth) is represented in by the red line. The number of iterations varies from 200 iterations until to 4000 by steps of 200. The results are displayed in figure 5.5:

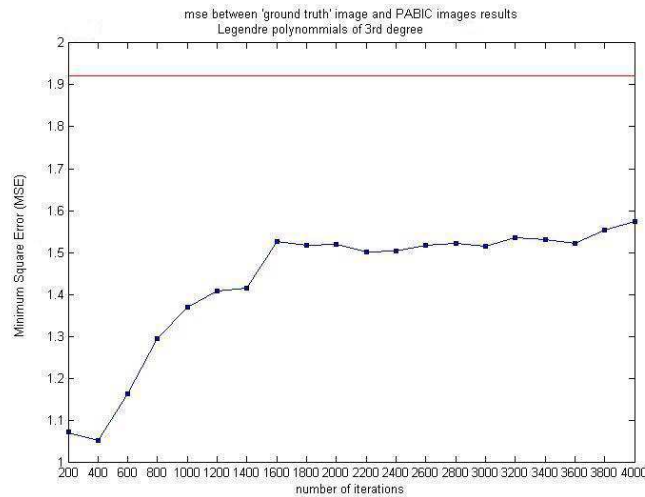


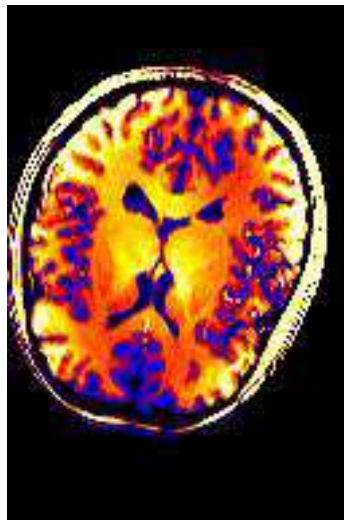
Figure 5.5: Evolution of the  $p$ -vectors while increasing the number of maximum iterations allowed.

In this figure, we see that when increasing the number of iterations permitted, the Minimum Square Error (MSE) also increases. The increasing is nearly linear with the number of iterations until 1600 but then it reaches a nearly constant value. That means there is an internal criterion in PABIC which stop the simulation when

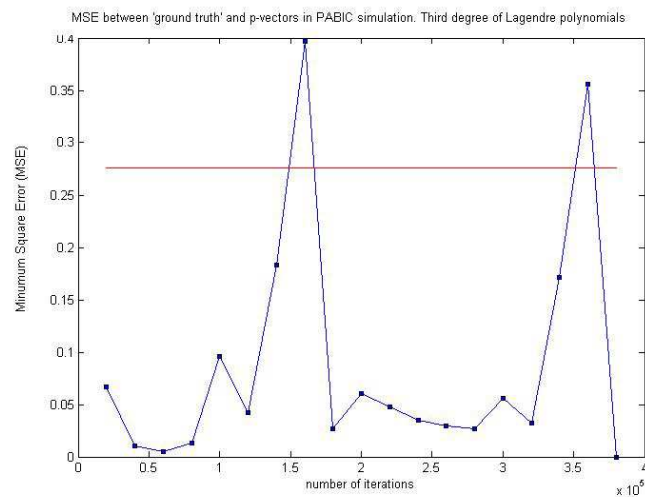
<sup>4</sup>The imaginary line in wich the surface coil is transmitting and receiving signal.

it reaches an acceptable result, even if the number maximum of iterations has not been reached. Nevertheless, we notice the result is not acceptable neither. In fact, PABIC stop running the simulation, because the result obtained is the best it can achieve (even if it is not good).

However, we can suppose that the bad results obtained in our second trial are due to the fact that PABIC is working in a transitory regime. "Transitory regime" because with this low number of iteration, PABIC demonstrate to not be able to reach a global minimum of the energy function, but a local one instead. Keeping the same parameters, we tried to improve the MSE by increasing the number of iterations allowed. We start computing the correction up to 40000 iterations. The results are displayed in the next Figure.



(a)



(b)

Figure 5.6: 2D human brain image corrected with PABIC (a) and the evolution of the p-vectors while increasing the number of iterations up to 40000 (b).

We notice, the MSE had been improved (avoiding the aberrant measures ob-

tained for 150000 and 300000 iterations). Nevertheless, the correction is not good enough as we can see in the Figure 5.7 (a). The intensity all over the tissues is not homogeneous, so we cannot say PABIC is correcting it.

At this point, we get really sceptical about if PABIC is capable to correct an 7T MRI acquisition. As said in Chapter 3.1, the bias is assumed to be smooth and slow variant when the magnetic field applied in the acquisition is lower than 3T, but it does not behave in this way in high-field acquisitions. PABIC lays in this assumption, so it performs pretty good bias corrections in low-field acquisitions but not in higher fields. However, some other test had been performed. In this case, with a 3D image.

## 5.2.2 Correcting a 3D Human Brain Image

As seen in Chapter 4.1, PABIC presents other abilities. It is capable to correct the bias field in the 3D space<sup>5</sup> for acquisitions under 3T, so we try to test the method working full power for 7T acquisitions.

A 3D MRI acquisition is a group of different 2D correlative slices . In our case, the correction was performed over a 3D volume consistent in 128 slices of 192x192 pixels per slice.

We have to notice, that working over a 3D image will increase the computation time. Actually, we have  $N$  slices of 192x192 so the time will be increase by this factor, where  $N$  is the number of slices.

For achieve this corrections, the same parameters were set in PABIC utility, allowing until 500000 iterations. The class-means and the class-sigma remained the same as the case of 2D correction. In this case, the time elapsed in simulation was 40 minutes, but the correction was not good. As we can see in Figure 5.7, where one single slide is shown:

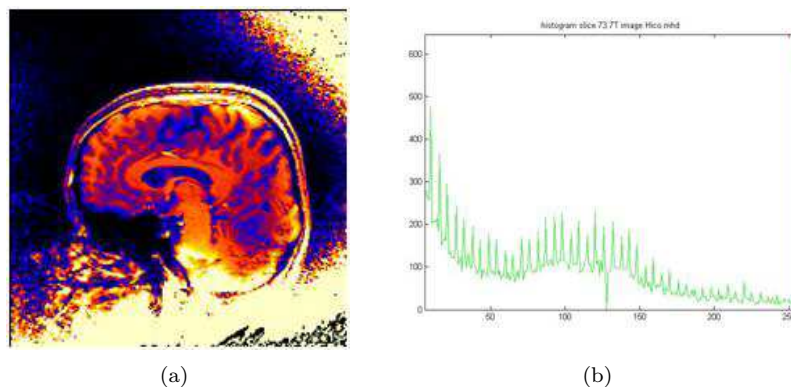


Figure 5.7: Slice of a 3D volume human brain image corrected with PABIC (a) and its intensity histogram (b).

The image is still corrupted by bias and the histogram shows the imperfect correction. The three main classes are not discernible as the maximum values of each gaussian are nearly the same, even if they represent three different kinds of matter.

<sup>5</sup>Remember that an MRI acquisition translated into the r-space is corrupted in all directions.

To plot the vertical and the horizontal profile lead us to clarify this aspect. In figure 5.8, these plots are represented. In fact, here we see the shape of the profiles are specially variant. This let us assess that the bias field in a  $7T$  acquisition has not any smooth variation. Besides, bias affected the image much more than noise (even if we can see the noise artifact if the take a look at higher frequencies). Besides, we can realize, looking at the vertical section that the maximum of the image is not exactly situated in the border of the image but a little bit further than that. This fact will lead us to have a high frequency discontinuity in the image, and is showing (again) that we do not have smooth variation of signal intensity, but a higher one, otherwise.

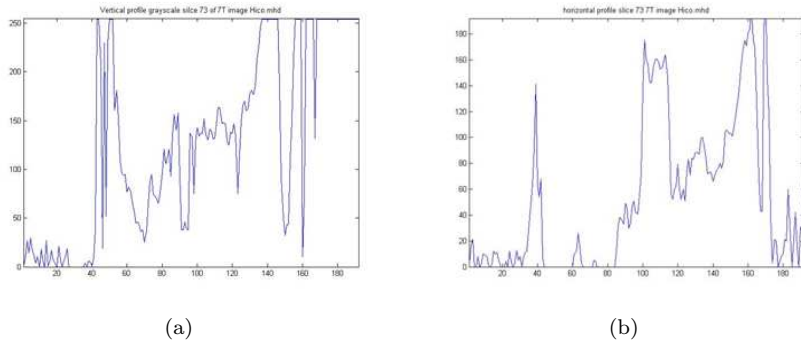


Figure 5.8: Vertical (a) and horizontal (b) profiles of gray values of one slice of a 3D human brain acquisition at  $7T$  after PABIC correction with third degree of Legendre polynomials.

In Figure 5.9, we present the correction achieve in a  $3D$  volume of a human brain acquisition over  $7T$ . The central slices had been selected as they present more information than the lateral ones. Besides, the signal-to-noise ratio is higher in the center (as we have seen in Chapter 2, and smaller in the periphery of the brain, so that, in this central slices we are supposed to have better contrast. In this serial of images, but can see the bias correction is not achieved.

### 5.3 The Low Pass Filter Correction

The Low-Pass Filtering method is a bias correction method based on the assumption that the bias remains in low-frequencies of our image and therefore can be estimate by low-pass filtering our corrupted image. Then, the correction is performed by dividing the original image by the filtered one.

Actually, is we recall the signal intensity model seen in Chapter 3.1, that represent the image in the  $k$ -space as:

$$s(\underline{x}) = o(\underline{x})b(\underline{x}) + n_{RM}(\underline{x}). \quad (5.4)$$

we can observe the frequency behavior by calculating its Fourier Transform:

$$\mathcal{F}(s(\underline{x})) = S(\underline{k}) = \mathcal{F}(o(\underline{x})b(\underline{x})+n(\underline{x})) = \mathcal{F}(o(\underline{x})b(\underline{x})) + \mathcal{F}(n(\underline{x})) = \mathcal{F}(o(\underline{x})) * \mathcal{F}(b(\underline{x})) + N(\underline{k}).$$

The low-frequency distortion is convoluted with the ideal signal, and it seems the bias can not be removed by making the convolution with low-pass filter kernel. However, as we still suppose the bias artifact in the low-frequencies it seems that

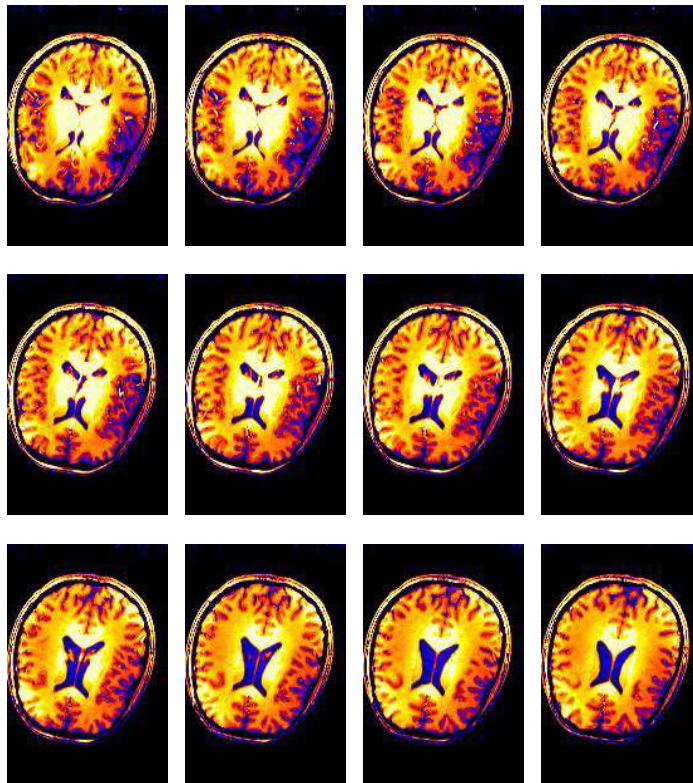


Figure 5.9: Central slices of the PABIC correction of a 3D human brain acquisition over  $7T$  (from top to bottom, first row slices 90 to 93, second row slices from 94 to 97 and last row, slices from 98 to 101).

filtering by a Gaussian filter (specially used in blurring images) or with a Median filter, we can achieve good results. In fact, those two filters had been tested and the results are displayed in this section.

Recall that the Gaussian filter is a wide used filter in signal processing. Gaussian smoothing is often applied because the noise or the nature of the object observed might be of a Gaussian probable form. In electronics and signal processing, a Gaussian filter is a filter whose filter window is the Gaussian function

$$x \mapsto \sqrt{\frac{a}{\pi}} \cdot e^{-a \cdot x^2}, \quad (5.5)$$

or with the standard deviation as parameter

$$x \mapsto \frac{1}{\sqrt{2 \cdot \pi} \cdot \sigma} \cdot e^{-\frac{x^2}{2 \cdot \sigma^2}}. \quad (5.6)$$

Mathematically, a Gaussian filter modifies the input signal by convolution with a Gaussian function; this transformation is also known as the Weierstrass transform. Gaussian filters are designed to give no overshoot to a step function input while minimizing the rise and fall time (which leads to the steepest possible slope). This behavior is closely connected to the fact that the Gaussian filter has the minimum possible group delay.

Note the Gaussian filter gives more weight to the current pixel position and then tapers the weights as distance increases according to the Gaussian formula. By weighting a pixels contribution to the final pixel value this filter can better preserve edges than the mean filter which specifies equal weights to all pixels within the filter window.

Whereas, the median filter is specially useful for removing outliers (that is, extreme pixel values). It used 'sliding neighborhoods' to process an image, that means it determines the value of each output pixel by examining and  $m - by - n$  neighborhood around the corresponding input pixel as the median value of them.

The goal of this filtering is to determine quantitatively which was the best method for low-pass filter a  $7T$  acquisition in order to palliate the bias field. The performance of the filter solution is simple:

$$CorrectedImage = AmplitudeFactor \times \frac{HighContrastAcquisition}{FilteredImage}. \quad (5.7)$$

The test was performed by consecutive filtering the target image changing the variance and the window size of the filter. The validation is achieved by computing the Mean Square Error (MSE) between the corrected image and the ground-truth. This ground-truth had been computed by dividing two different acquisitions obtained with different protocols. That is, by dividing one MPRAGE acquisition by one FLASH acquisition. Recalling Chapter 2, Section 2.5, we must clarify that we are actually diving one high-contrast image (MPRAGE) by one obtained with a low-contrast protocol (FLASH)<sup>6</sup>.

Actually, the main goal of this experiment is to have a 2D map showing the effects of varying this parameters, and find the best option for bias correction by

---

<sup>6</sup>This method had been developed by Xavier Peña Piña at the EPFL, with the collaboration of Siemens Research Group site at the CIBM, Lausanne.

low-pass filtering.

This time, the original image has not only been masked by setting a simply threshold. Besides, after the threshold that let us avoid the background (as seen before), the image was 'skull stripped' using BET<sup>7</sup> algorithm. Skull stripping commonly refers for *Intracranial segmentation*, and it segments the brain tissue (cortex and cerebellum) from the skull and non-brain intracranial tissues in magnetic resonance (MR) images of the brain. So that, it isolate brain from extra-cranial or non-brain tissues. Skull stripping is an important preprocessing step in neuro-imaging analysis because brain images must typically be skull stripped before other processing algorithms such as registration, tissue classification, or bias field correction can be applied.

Besides, the masked and skull stripped image has also been de-noised. We must say that In order to illustrate this part of the process, we take a single slice of the 3D volume (see Figure 5.10). So that, the images used for this test are:

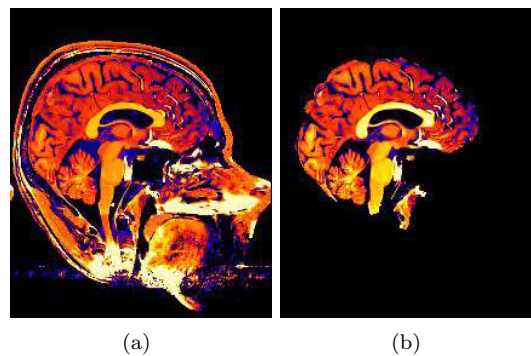


Figure 5.10: 7T MPRAGE acquisition of human brain masked by direct threshold (a) and same acquisition skull stripped and de-noised (b) . (Both in sagittal view).

The skull-stripped and de-noised image, (b), when filtered, is compared to our ground-truth. And this ground truth is, by its axial view (see Figure 5.12).

In resume, the processing chain for this low pass filtering method is shown in Figure 5.11.

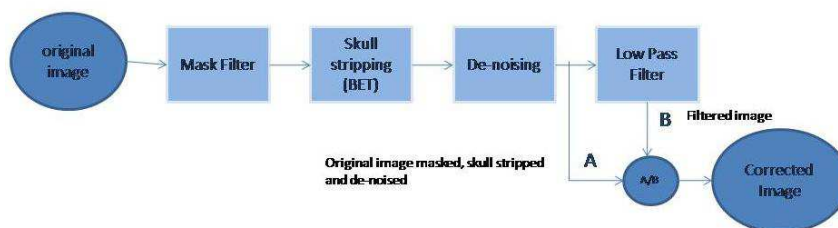


Figure 5.11: Block diagram of the LPF method proposed

<sup>7</sup>BET algorithm belongs to the FSL Software Library. FSL is a comprehensive library of analysis tools for FMRI, MRI and DTI brain imaging data. FSL is written mainly by members of the Analysis Group, FMRIB, Oxford, UK. It can be found in <http://www.fmrib.ox.ac.uk/fsl/fsl>

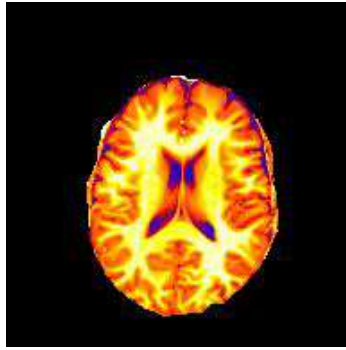


Figure 5.12: Ground truth for correction goodness' quantitative comparison. One single slice of a 3D volume in its axial view. Ground truth obtained by diving MPRAGE acquisition by parallel FLASH acquisition

Let's start with the process. In the image we can note even in the inner part of the brain there are some morphological peculiarities than can make impede the correct estimation of the bias and, thus, its correction. SO our aim is to remove them before the estimation.

The first step is to mask the image by direct threshold. This masking process, a part for removing the background, can be used to remove high frequency artifacts in the image due to tissue transitions. This tissue transitions are characterized by having high gradient value. Thus, one way to localize them is by computing the gradient of the image. With this process we can get some extra information than can help us in the correction. But, before computing the gradient of the image, a low-pass filter is applied as the artifact we want to erase are at high frequencies.

After that, the BET algorithm is applied (see [12]), so that we remain with the inner part of the brain, without skull. Finally, we apply and de-noising filter. At this point, our image is ready for our purpose: the extraction of the bias field by low-pass filtering.

### 5.3.1 Results and Validation of the Method

The first filter tried is the Gaussian filter. By changing the variance and the window size values, we consecutively filter the corrupted image. For each case, and following the hypothesis that the bias field is estimated by the low-pass filtering, we compute the division of the original image by its filtered sample (as shown in 5.3. After that, the Minimum Square Error between the ground truth and the correction calculated. So that, considering the variance values ranging from 1 to 25 and the window sizes moving from 1 to 80, the following results are obtained:

As we can see in the images, the time elapsed in simulation increases while increasing the window size of the filter. This is a result we should expect. In fact, this filter is applied to an image in a two phase approach. First the horizontal direction is filtered using the above filter in a similar manner to a convolution filter by taking each pixel in the image, centering the filter on that pixel (the middle value) and then multiplying the pixel values by the weight at each filter location followed by a final divide to get the resulting new pixel value. This process is then repeated vertically on the horizontally processed image to create the final image. So, growing window size, will grow the length of the convolution and, thus, the time of computation.

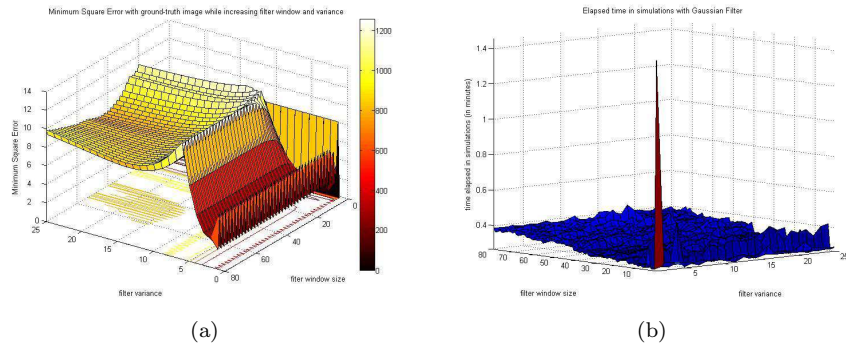


Figure 5.13: Evolution of the MSE between ground truth and image corrected by low pass filtering method when changing the variance and the window size of the filter (a) and evolution of the time elapsed in simulations (b). The low pass filter applied is the Gaussian filter. (variance values from 1 to 25 and window sizes from 1 to 80).

However, if we compare this time with the one needed to perform PABIC correction in the same image, we see the low-pass filtering is a faster method for correction. In fact, the mean time of computation in this case is around 2 minutes, whereas when running PABIC correction was around 14 minutes in a 2D image and around 40 minutes in a 3D one.

One consideration must be done at this point. Window size of the filter is normally related to the variance. Actually, it was not necessary to cover all the sigma values from 1 to 25 changing at each time the window size from 1 to 80. It should have been enough to change the variance from value 2 to 20 in steps of 2, and then, for each variance value, change the window size from  $3 \times \text{variance}$  to  $5 \times \text{varinace}$  in steps of the variance value. Nevertheless, the complete coverage has been done in order to plenty test the method.

If we focus now in the MSE graphic, we realize we do not get acceptable values for the Mean Square Error between the corrected image and the image assumed as ground-truth. Thus, we can achieve from here, the filtering by Gaussian filter is not enough for estimate the bias at high field acquisitions. However, we can see that considering variance values over 10 gives us a MSE up to 8, whereas if we constraint our filter with variance values around 5 can give us some acceptable results in the quantitative comparison with the ground truth. Thus, when low-pass filtering with a Gaussian filter, we must consider variance  $\sigma = 5$  and window size between the values  $\text{window} = (15, 25)$ .

After this trial, the Median low-pass filtering was tested for bias estimation and correction in  $7T$  MR images.

As said in the previous section, the Median filter uses 'sliding neighborhood' to determine the output pixel brightness value. Figure 5.14 shows an example of the median filter application, as in this case, habitually a  $3 \times 3$  median filter is used. The Figure 5.14 (a) presents the concept of spatial filtering based on a  $3 \times 3$  mask, where I is the input image and O is the output image. In Figure 5.14, the median value is determined by placing the brightness in ascending order and selecting the center value. The obtained median value will be the value for that pixel in the output image.

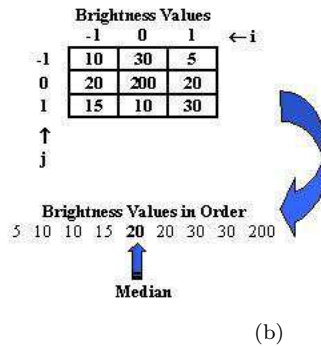
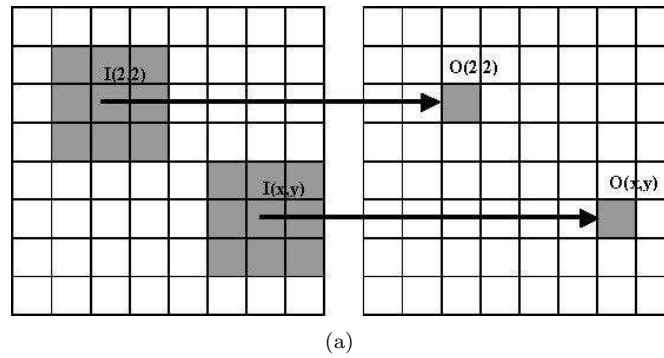


Figure 5.14:  $3 \times 3$  median filter operation. In (a) some samples of input pixel and its neighboring are displayed. The bright value of the output pixel is computed as shown in (b).

So that, an as the Median filter<sup>8</sup> is supposed to be a more robust method than the traditional linear filtering, because it preserves the sharp edges, we expect to achieve a better bias estimation than when applying Gaussian filtering.

Nevertheless, the tests with Median filtering did not give better results. Actually, the main problem of the median filter is its high computational cost (for sorting  $N$  pixels, the temporal complexity is  $O(N \log N)$ , even with the most efficient sorting algorithms). When the median filter must be carried out in real time, the software implementation in general-purpose processors does not usually give good results.

Besides, even having the complexity of the algorithm increased as well as the computation time by a factor of  $O(N \log N)$ , the correction is neither good in terms of intensity homogeneity.

### 5.3.2 Summary of Bias Correction with Retrospective Methods

Two different retrospective methods for bias correction in  $7T$  MR acquisitions had been tested in this section: the Parametric Bias Correction (PABIC) and the Low

<sup>8</sup>Median filter is the nonlinear filter more used to remove the impulsive noise. Median filter is a spatial filtering operation, so it uses a 2-D mask that is applied to each pixel in the input image. To apply the mask means to center it in a pixel, evaluating the covered pixel brightness and determining which brightness value is the median value

Pass Filtering approach.

Even if none of the methods plenty achieve the bias correction desired in the image, one comparison between them can be done.

PABIC method is good to deal with multi-class images, which is one of the main drawbacks when trying to correct the bias directly from a brain MR image. This pretty good behavior is due to its parallel segmentation process (which is not done with the low pass filtering approach). Besides, PABIC parametrizes the bias field, giving it in terms of the  $p$ -vectors so it can be recursively run, giving them as a initial point for the next step. Otherwise, the computation time became an important drawback when using this method for bias correction in 3D images. The time elapsed in simulations are quite acceptable for 2D acquisition but not for 3D images, as it increases nearly exponentially. Nevertheless, it can be reduced by forcing PABIC to start with a certain p-vector value (normally our ground truth vector). However, even in this case, it does not reach good results as it is incapable of found a energy global minimum, remaining most of the times in a local minima of the energy function. This is not the case for the Low-Pass filter approach.

The main advantage of the Low Pass Filter for bias correction is that this method is much faster than PABIC (time elapsed in computation with this approach is nearly then time faster than PABIC). Besides, the simplicity of the algorithm makes him a good option for image bias correction. However, the correction achieved by this filtering is worse than the obtained with PABIC. In fact, this method does not parallel segment the image so is harder to find the tissue boundaries even if a gradient filter is used. Actually, the LPF method is good for correcting single-class image<sup>9</sup>. Nevertheless, its strength is weak when a multi-class image are considered.

Despite what we could had imagine before trying the correction by one of those retrospective methods, nor PABIC neither the Low Pass Filtering approach, perform good bias correction in  $7T$  acquisitions. It is due to the fact that the assumptions of smoothness an slow variation are no longer valid. This leads us to say that a method to correct the bias directly from the acquisition with no other information is not suitable for acquisitions at high field strength (i.e. over  $7T$ ). Some additional information is needed for achieve an acceptable correction in terms of visual inspection and histogram computing.

Actually, as we can see, there is not only bias in the low-frequency band, but a mixture of undesired bias field and important information. Both are difficult to separate without no a priori information.

Following this idea, a new method is presented in next Chapter. This method take profit from the acquisition of an RF map at the same time of the image. This amp gives us information about the distribution of the field and the flip angle inside the brain, thus, information about the bias field added to the image.

---

<sup>9</sup>Recall for further information the master thesis *Bias Field Correction in Magnetic Resonances of a Rat Brain* [40]

## Chapter 6

# A New Prospective Solution Using the RF Mapping

The main goal of this Master Thesis is to estimate and eliminate the bias field added in the MR acquisitions obtained at high fields (over  $7T$ ). In previous sections we have proved the impossibility of achieve this correction directly from the corrupted image. The bias field behavior in high field acquisition avoid this fact. Actually, it cannot be seen as an spatially sooth and slow variation. Thus, other information is needed for this purpose.

Following this aim, we present a new method, based on the acquisition of a RF map after acquiring the image. Note here we have a compromise. As said in Chapter 3.1, the acquisition time is a critical parameter when imaging living tissues. The patient must stay longer inside the magnet, at this fact present several drawbacks:

- The patient should avoid moving for acquiring this map in the most accurate way. If he moves, more artifacts will be added to the image. Otherwise, not moving is not easy, as the magnet is not a comfortable place to lay on.
- Each living tissue presents an maximum absorption rate that cannot be exceed. Actually, when acquiring an MR image, we are applying a magnetic field over the tissues (recall Chapter 2) so we must be careful on not expose the tissues more time that they can stand.

Actually, with this additional acquisition we are trying to get enough information to proceed successfully to the bias correction. And, for  $7T$  acquisitions, where the bias pattern is not already defined, this is the best possibility for this purpose.

$B_1$  mapping is crucial for the understanding of  $B_1$  inhomogeneity patterns and for quantitative studies such as  $T_1$  ad  $T_2$  measurements. Because there are different sources of variation of the field behavior inside the brain,  $B_1$  mapping add confidence and give important insights into the interpretation of the magnitude images.

It is clear, at this moment, that even susceptibility artifacts appears in the acquired images, in there we can also see substantial signal variability due to the  $B_1$  inhomogeneity. Actually, as Trong-Kha et al. assess, *regions of low signal corresponds, directly, to regions with low flip angle and/or low receive sensitivity. The flip angle variability affects not only the SNR but also the image contrast* [34].

Considering different types of acquisition, the effect of the bias field changes. It has been demonstrate that the image contrast will be more severely affected by

flip angle variation on  $T_1$  weighted images. And,  $B_1$  inhomogeneity and the resultant spatial variability of the flip angle become progressively more problematic in multi-pulse sequences (as the MPRAGE). For small flip angle images, the intensity distributions are approximately symmetric about the centerline of the coil. With increasing flip angle, the symmetry in the signal intensity pattern disappears, behavior caused (as the reader can imagine) by the asymmetry in transmission and reception in the data acquisition process.

So that, to quantify this  $B_1$  inhomogeneity, we can compute a map of the flip angle and a map of the receive sensitivity. Different methods had been proposed in literature for this achievement. In [18] three methods are enumerate:

1. Increment transmitted reference amplitudes and fit as assumed signal behavior.
2. Acquire several echoes and calculate the RF distribution by their proper combination.
3. Use preparation pulses or additional pulses in various sequences.

All of this methods are implemented in  $2D$  due to time constraints, but in [2] we can see a method based in two simultaneous acquisitions which is the one used for our purpose. Is not extremely difficult to compute those two maps (the flip angle map and the receive sensitivity one). Following Siemens' protocol for flip angle map computation, two series of low-resolution images are computed with  $T_R \gg T_1$  and flip angles  $\alpha_0$  and  $2\alpha_0$ . The acquisitions are one *Spin-Echo* sequence and one *Stimulated-Echo*. In this case, the signal intensity at the pixel  $(x, y)$  can be written as:

$$S_\alpha(x, y) = \rho(x, y)r(x, y) \sin[\alpha(x, y)], \quad (6.1)$$

and

$$S_{2\alpha}(x, y) = \rho(x, y)r(x, y) \sin[2\alpha(x, y)] \quad (6.2)$$

respectively, where  $\rho$  is the proton density,  $r$  the received sensitivity and  $\alpha$  the local flip angle. A **flip angle map** can be computed from the signal intensity ratio of the two series as follows [34]:

$$\alpha(x, y) = \frac{S_{2\alpha}(x, y)}{2 \cdot S_\alpha(x, y)}. \quad (6.3)$$

Then, a map of the product of the proton density and the receive sensitivity can be computed from the flip angle map using 6.1:

$$\rho(x, y)r(x, y) = \frac{S_\alpha(x, y)}{\sin[\alpha(x, y)]}. \quad (6.4)$$

Finally, a measure of the **receive sensitivity** can be generated from this map by low-pass filtering (with a  $2D$  boxcar filter) and normalizing between 0 per cent and 100 per cent.

In principle, two measurements with different nominal flip angle are sufficient for determine the flip angle value  $\alpha$ . However, since the resulting flip angle is determined from the linear regression of results of all measurements, the acquisition of the RF maps with more nominal angles reduces the sensibility of the calculate  $\alpha$  values of the noise [18]. So, we must prevent that this method for calculate the flip angle and sensitivity map from two different sets of images with nominal flip angles

$\alpha_0$  and  $2\alpha_0$  is theoretically accurate for local flip angle  $\alpha$  ranging between  $0^\circ$  and  $180^\circ$ . If the local flip angle exceeds  $180^\circ$ , this method can no longer determine the correct flip angle. Actually, signal intensity not only decreases in regions with small flip angles but also in regions with angles larger than  $90^\circ/180^\circ$ , where the spins are over-flipped.

At this point, it is almost clear that to correct effects of the RF inhomogeneities in 3D data sets it is necessary to have knowledge of the field distribution inside the sample. Thanks to the Siemens' acquisition protocol we can obtain two different maps from this  $B_1$  distribution, the (1) **magnitude  $B_1$  map** and (2) the **flip angle map**, which is the relative spatial phase pattern for received and transmitted field.

## 6.1 Magnitude $B_1$ Mapping and Flip Angle Mapping

In Chapter 3.1, we have presented the way of modeling the signal intensity in each voxel of the image. Assuming that for each voxel we can explain signal intensity modulation as:

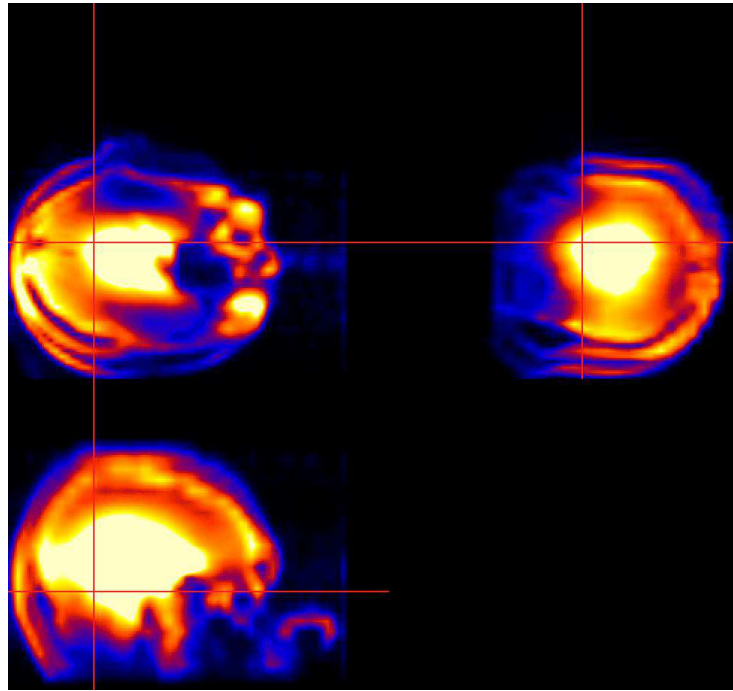
$$I \propto \rho \sin(V|\hat{B}_1^+|\gamma\tau)|\hat{B}_1^-|, \quad (6.5)$$

where we can see the influence of the transmitted field ( $|\hat{B}_1^+|$ ) and the received one ( $|\hat{B}_1^-|$ ).

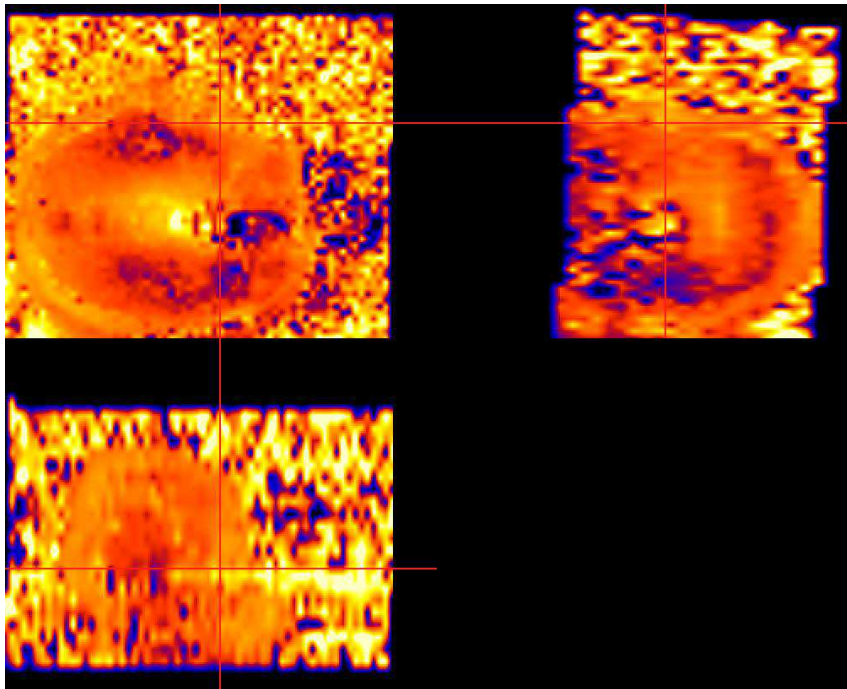
The way to determine the  $|\hat{B}_1^-|$  and calculate its map is by fitting the modulation of the signal intensity with a sinusoidal function. Once this map is calculated is straightforward to determine the actual flip angle at each pixel location of an *GE* acquisition [37]. Actually, in [37] an experimental examination of the 7T RF coil interferences between different coil elements is performed, giving special importance in phase spatial distribution. In Appendix C the main formulas are transcribed for interested readers.

An example of this two maps can be seen in Figure 6.1, where Figure 6.1 (a) in the  $B_1$  magnitude map and the Figure 6.1 (b) shown the flip angle map. In this approach, only the flip angle map had been used as it the less corrupted by inhomogeneities.

In this images, we can suppose (as Jinghua prove in [17]), that any inhomogeneity in the flip angle map is due only to the  $B_1$  inhomogeneity. In fact,  $B_0$  inhomogeneities can impact the signal intensity, but do not directly influence the flip angles obtained. In this assessment lean this new approach to bias correction. We know the flip angle map is only corrupted by the  $B_1$  inhomogeneity so, each inhomogeneity in this map will be due to this artifact. Thus, this flip angle map is, simply, a map of the inhomogeneity we get when imaging a living tissue.



(a)



(b)

Figure 6.1: Single slice representation of the computed B1 magnitude map (a) and computed flip angle map (b) from an human brain at  $7T$ .

## 6.2 Bias Correction using the RF Mapping

As seen before, for correcting an high-field MRI acquisition we need some additional information. Until now, and for low-field acquisition, the correction was performed directly from the corrupted data by estimating the bias due its smoothness and slow variation. Nevertheless, this direct correction cannot be achieved in high-field acquisition. Some additional data is needed. And, following this aim, we present a method based on the double acquisition of an image and the RF map (also know as flip angle map).

The test were performed over one MPRAGE 3D acquisition supplied by the Siemens Research Center in the CIBM. A  $B_1$  magnitude map and a flip angle map were also supplied. The transverse (axial) MPRAGE acquisition is composed by 160 slices of  $216 \times 256$  pixels each. This image is presented in Analyze 7.5 format as it is an high dynamic range image (HDR). In the Analyze coordinate system, with this acquisition we get:

1. 160 transverse slices laying on the  $xy$  plane, each of  $216 \times 256$  pixels.
2. 216 sagittal slices laying on the  $zy$  plane, each of  $256 \times 160$  pixels.
3. 256 coronal slices on the  $zx$  plane, each of  $216 \times 160$  pixels.

The test wee performed over a Intel(R) Core(TM)Duo CPU 6600 @2.40GHz, 1.98GB of RAM, but in this case, the time elapsed in simulation was not computed. This time is much higher than the one needed for retrospective corrections, but, in contrary, the correction performed in piecewise better. One consideration must be done: these tests were performed over a 3D acquisition of high dynamic range so that, the amount of data is much bigger than the one used for validate other correction methods. Thus, having increased the time of computation is specially due to this fact.

The algorithm for the correction is based in nearly the same concept used for correcting image with low-pass filtering. The corrupted image, after been masked, skull-stripped and de-noised is divided by the flip angle map and finally multiplied by the received field contribution. This last multiplication is performed because when dividing the corrupted image by the flip angle map, we loose some contrast. A block diagram can be seen in Figure 6.2:

## 6.3 Results and Validation of the Method

Following the algorithm of bias correction, the MPRAGE acquisition was masked by setting a threshold. After that, the skull stripping was performed using (as in the case of the Low Pass Filter approach) the BET algorithm from the FSL Library. We must say that this method for skull stripping is not the only one. Actually in the literature, we can find several methods for brain extraction that seem to work even better that BET algorithm. The choice of this one was done because BET algorithm is a method fully-automatized and fast and easy to use. Even thought, we might have test some others. However, due to time constraints, only this one was tested. It means that some other protocol can be used that might improve the result or the time of computation. This can be seen as a future work for the improve of the algorithm.

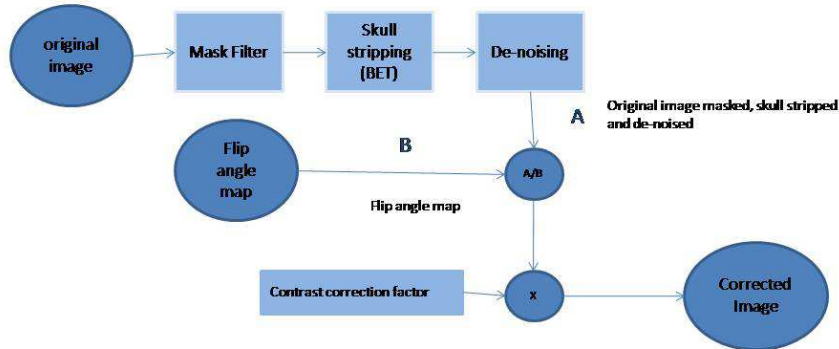


Figure 6.2: Block diagram of the method proposed. Bias Correction by RF mapping

Once the image is masked and skull-stripped, it is de-noised to facilitate the correction. Actually, by de-noising we erase some unwanted effects that might be confused as bias. We must say that the flip angle map was also masked for removing all the background. Besides, we cannot forget the importance of having the images well registered. Actually, we are dividing pixel-by-pixel one image by its corresponding flip angle. If the images are not accurately registered, we might be dividing one pixel by flip angle value of the neighboring pixel and the results will be distorted.

The correction was performed over a 3D volume. Nevertheless, to illustrate this section, only several slices of the volume are presented. In figure 6.3, the three views (axial, sagittal and coronal view) of a single slice of the volume used for the test are represented:

The result of the algorithm is seen in Figure 6.4:

The validation of this method had been performed only by visual inspection. As we can see in the image 6.4, even the bias correction is not totally performed, the image had been corrected in intensity inhomogeneities. We are still missing some good results in the hypothalamus and the temporal lobe. This can be due to the fact that the acquisition of the flip angle map was not plenty co-registered with the MPRAGE acquisition. In fact, for achieve this registration, the flip angle map was switched by a 10 degree angle. And when we are talking about one 'angle representation' image, this fact is not negligible.

This fact can also explain the lost of contrast of the image. Even after multiplying the image by the contrast correction factor which is the contribution of the received field to the image (i.e.  $B_1^-$ ), the contrast is not well recovered. Nevertheless, the improvement of this method in comparison with the retrospective ones

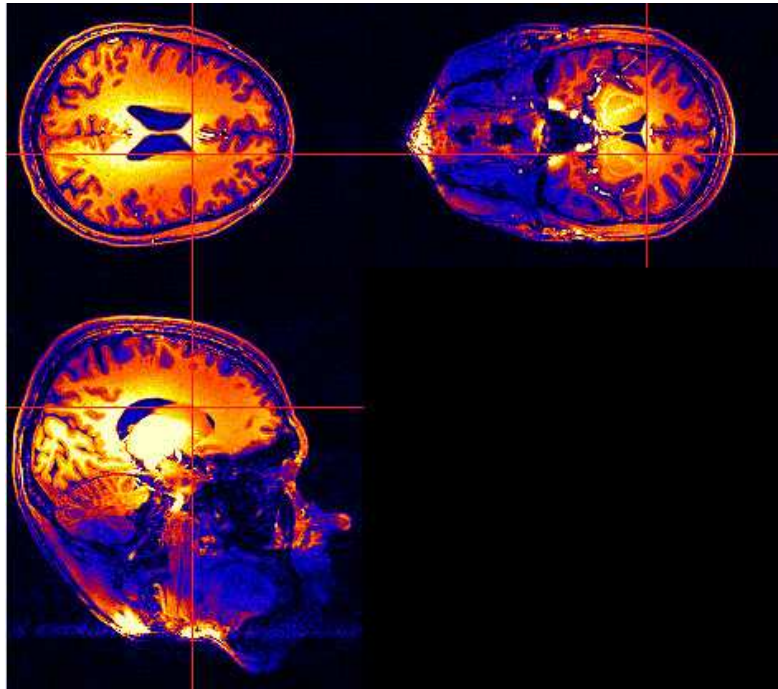


Figure 6.3: Axial (transverse), sagittal and coronal view of a single slice of a 3D volume MPRAGE acquisition of 216x256x160 pixels before the correction using the RF mapping.

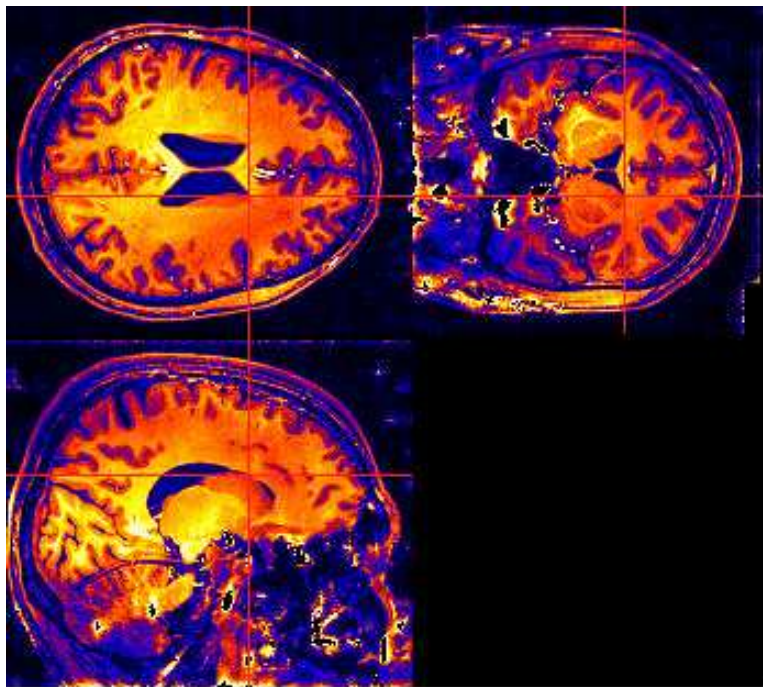


Figure 6.4: Axial (transverse), sagittal and coronal view of a single slice of a 3D volume MPRAGE acquisition of 216x256x160 pixels after the correction using the RF mapping.

analyzed in this report, is that the brightness of the image seems to be more homogeneous than in the other cases. We have been able to erase the bright spot in the middle of the image, attenuating its value and, besides, we have achieved a better homogeneity in almost all the image (even though we have lost contrast).

This is not a perfect result, but, however, it is an encouraging one. In fact, after having tried several methods for achieving this bias correction which was the main goal of this Master Thesis we realized that none of the actual ones work, so, a new method is needed. Bias Correction by using the RF mapping can be this needed one. As a future work, one improvement of this method can be tried, in order to completely parametrize the bias inside the brain, so that will allow the total correction of the bias without contrast loss.

## 6.4 Summary of A New Prospective Solution Using the RF Mapping

In this Chapter a new prospective solution has been presented. This new approach leans on the need of having some additional information for properly achieving the bias correction in  $7T$  MRI acquisitions.

Actually, for low-field acquisitions, we are able to correct the bias directly from the corrupted data, as this bias has smooth and slow varying behavior so that it lies on the low-frequencies of the image. Due to this fact, Low-Pass filtering can be a good and fast approach for this purpose.

In high-field acquisition, the assumption made for the bias is no longer valid, so some additional information is needed to perform the correction. The approach presented in this section, takes profit of the acquisition (at the same time of the image) of a RF map (or flip angle map). This map is related to the angle of precession of the spin in the living tissue and, therefore, any inhomogeneity in this map will be showing the inhomogeneity due to the bias field.

Some tests had been performed and even the results are not completely perfect, they give a new line of investigation for future work on bias correction in  $7T$  acquisitions.

## Chapter 7

# Conclusions and Future Work

The aim of this project was to remove the bias distortion, so called *bias field* or *intensity inhomogeneity*, from MRI images of human brain acquired with  $7T$  MR machines. The ultimate goal was, obviously, to supply the medical community with a tool which could allow them to diagnose, in a reliable way, possible human brain diseases as well as help them understand its behavior by having the chance of giving and accurately insight into the physiological condition of the brain.

The first attempt in this way was to test reliable methods in bias correction under  $3T$  that were plenty proved in this achievement. The PABIC and the Low-Pass Filter were tested. Both rely in the assumption of smoothness and slow variation of the bias field along the images. Even its capacity of extrapolate the bias all over the image (i.e. the region corrected can be bigger than the region measured to estimate the bias), none of them can completely ensure the success in bias estimation and bias correction. Actually, as the bias does not have smoothness behavior anymore it cannot be approximate by Legendre Polynomials or other smooth basis functions. So that, PABIC present several problems to reach the global minimum of energy needed when estimating the bias. Besides, the bias field presents a multiplicative effect over the image intensity that cannot be transformed in additive by log-transformation. This avoid us getting good results by low pass filtering the image by Gaussian or Median filters, which was a point we want to prove following the work done at the EFPL by Xavier Peña Piña over  $9.4T$  acquisitions in rat brains [40].

This fact can be seen as the main contribution of this master thesis. We have demonstrate that the methods for performing bias field correction in acquisitions with field less than  $3T$  are no longer useful for correcting  $7T$  acquisitions. All the conclusions and results are based in the fact that at  $7T$  the bias can not be assumed as a slow and smooth variation all over the image.

Actually, the main drawback is that, when increasing field strength (specially if we work with **high field acquisitions** ( $> 7T$ )), the bias field starts having a **wave behavior** that makes impossible its approximation by an smooth function as it is strongly dependent in the dielectric effects, and the conductivity of each tissue in the brain. Artifacts due to  $B_0$  and  $B_1$  inhomogeneity are severe in ultra-high magnetic field MRI and experimental and/or numerical mapping of the  $B_0$  and  $B_1$  inhomogeneity is important in identifying their origin. Detailed characterization of these effects is an important step in the development and assessment of  $B_0$  and  $B_1$

inhomogeneity correction methods. In this fact lean the new prospective approach presented in this Master Thesis.

The idea of this method is to *acquire extra information during the imaging process*, so that it can help in the bias correction. The main advantage of it (when comparing with other approaches) is that this correction, if well used, could be more consistent than the other ones. Actually, it relies in an analytical approach of the intensity inhomogeneity at high fields strengths. In fact, we have seen during this report that correcting the bias field directly from the corrupted data has serious limitations (specially at high-fields).

Nevertheless, this feature has some drawbacks. Its is computationally complicated (specially if we compare it with the Low-Pass Filter approach) as we are dealing with a big amount of data. And, at this point of the research, we have not been able to assure neither in this case a perfect bias correction in  $7T$  acquisitions. However, despite this fact, the results are enough encouraging to keep working in this line.

In this report we actually present a draft for a method which can combine the two lines of investigation in bias correction we found nowadays: the prospective and the retrospective methods. And, as a future work, some new improvements can be done as a future work.

- A accurate parametrization of the bias should be deeply studied so the  $B_1$  mapping can be fully defined. We cannot forget (as said in Chapter 5.1) that the image registration becomes crucial at this point. When comparing the image with its RF map, we need all the pixel/voxel to have perfect correspondence in both images.
- Improve the steps prior to the image division. That is, improve the skull stripping and the de-noising, as well as the masking. In fact, the less artifact we get in the image (even if they are not due to the bias) the better results we can get. Several methods are proposed in the literature in this sense, even we had only tried the BET algorithm due to time constraints.
- To combine previous estimation and post-correction force us to get specially knowledge of the nature of the images (both MPRAGE acquisition and RF map). An effort combination between physics and signal processing research groups had permitted us to outline this new approach. However, keep this line of research could lead us to successfully estimate an remove the bias in this high field acquisitions.

As the last point of this Chapter, note that, even if this report focus in MRI acquisition of human brains images, the bias appears in all MR imaging techniques, whereas we are imaging the brain or other parts of the body. So that, the conclusion assessed for the specific case of the brain, can be extrapolate to other MR acquisitions. So that, erasing the bias in high field acquisition could give us, not only a good insight of the brain but the whole human body.

# Appendix A

## Radio-frequency Power Requirements of Human MRI

The values obtained in this Appendix rely on the study carry out by L.Tang in his paper [32]. The values had been obtained by a simulation model, a 16-element TEM resonator based on multi-conductor transmission line theory loaded by an anatomically detailed head mesh.

### A.1 Power an SAR Calculations

The input power from the RF coil can be written (deriving it from Maxwell equations) as:

$$P_{input} = P_{abs} + P_{rad} + \frac{\sigma}{2} \int \int \int_v |\vec{E}|^2 dv + \frac{1}{2} \int \int_s (\vec{E} \times \vec{H}^*) ds, \quad (\text{A.1})$$

with  $P_{abs}$  and  $P_{rad}$  the absorbed and radiated power,  $\sigma$  is the conductivity and  $\vec{E}$  and  $\vec{H}$  are the electric and magnetic fields respectively.

The RF power absorbed is related with the flip angle (as we have seen is linearly proportional to the circularly polarized component  $B_1^+$  we can only consider the absorbed power. So changing the continuous integration by summation we obtain:

$$Power = \sum_i \sum_j \sum_k \left[ \frac{1}{2} \sigma_{(i,j,k)} \times (E_{x(i,j,k)}^2 + E_{y(i,j,k)}^2 + E_{z(i,j,k)}^2) \right], \quad (\text{A.2})$$

where  $\sigma_{(i,j,k)}$  in  $[S/m]$  is the conductivity at the  $(i, j, k)$  location.  $E_x$ ,  $E_y$  and  $E_z$  are magnitudes of the electric field components in the  $x$ ,  $y$  and  $z$  directions and expressed in  $[V/m]$ .

The SAR is modeled as:

$$SAR_{(i,j,k)} = \frac{1}{2} \frac{\sigma_{i,j,k} (E_{x(i,j,k)}^2 + E_{y(i,j,k)}^2 + E_{z(i,j,k)}^2)}{\rho_{(i,j,k)}}, \quad (\text{A.3})$$

where  $\rho_{(i,j,k)}$  is the tissue density at location  $(i, j, k)$ . SAR has the unit  $[W/Kg]$ .

## Appendix B

# 1D Electromagnetic (EM) Theory for Wave Interference

At this point, it is proved that the highest  $B_1$  inhomogeneity that occurs in a sample when acquiring an MRI at high field is due to the wave behavior of the field inside the brain. Actually, as the sample dimensions represent a larger percentage of a wavelength ( $\lambda$ ), intermediate and far field effects, including wave propagation, become more important. At it is this presence which requires the use of the full-wave solution of Maxwell equations. In this Appendix, 1D theory is explored to explain the patterns of the interference sources in a phantom. It has been performed in [7].

Whereas the coil used are volume coils, arrays surface coils or single surface coil, the wave interference effect, appears when a sample is added in a MRI machine. And this interference, can be constructive o destructive.

The explanation is simple. When a sample is added, and due to the multiple air/tissue we find in the brain, the applied field will suffer numerous reflections, giving a multiple path pattern propagation. One example can be seen in figure B.1:

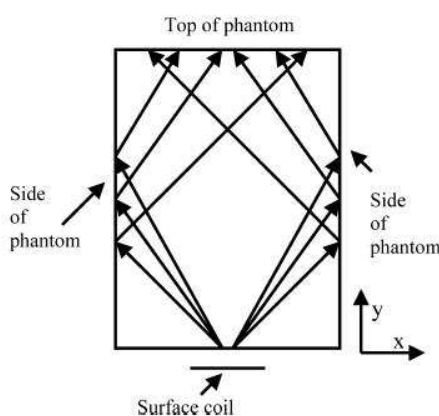


Figure B.1: Multiple propagation path in rectangular sample with large reflection coefficients at boundaries.

In this figure there are represented some of the possible paths where the wave would propagate. When getting at the boundary a reflection take place. If at this moment there is no phase difference between the incident wave and the reflected one,

we will get a constructive interference and the values of amplitude will be added. By contrary, if there is a 180 phase difference, the interference will be destructive and the two wave will cancel them out. Those 2 cases are the extreme ones but we can find all the intermediate ones that will cause different level of interference.

So, how we can determine the effects of sample properties and size in this propagation? Let us consider a plane wave traveling with normal incidence (that is to say perpendicular) to the sample considering  $B_0$  on the  $z$  direction, a linearly polarized  $B_1$  in the  $y$  direction and a wave traveling on the  $x$  direction. The sample is formed by four layers (and it can be extendable) with different physical and electrical properties (see fig. B.2).

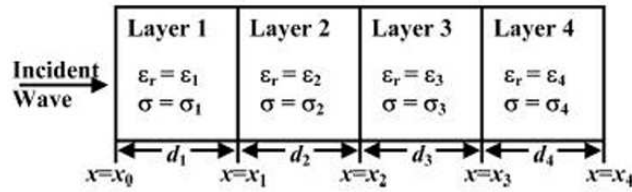


Figure B.2: Sample with four different layers and their physical and electrical properties.

Assuming the incident wave in a single direction  $\mathbf{B}(x_0) = B(x)\hat{y}$  (for facilitate the computation) we get a general form of the solution for the magnetic field  $\mathbf{B} = B(x)\hat{y} = B_{y0}h(x)\hat{y}$ .  $h(x)$  is found for solving the wave equation at each layer:

$$h_i(x) = C_i \cos k_i + S_i \sin k_i, \quad (\text{B.1})$$

with  $i = 1, 2, 3, 4$  and  $k$  the complex wave number defined by:

$$k_i = \alpha_i + j\beta_i. \quad (\text{B.2})$$

In equation B,  $\alpha_i$  represents the attenuation constant and  $\beta - i$  is the phase constant in the layer. The skin depth  $\delta$  is related to  $\alpha$  as  $\delta = 1/\alpha$ .

The coefficients  $C_i$  and  $S_i$  are found using the eight boundary conditions [33] at the interface between layers:

- Initial value at  $x_0$ .
- Continuity of  $E$  and  $B$  fields at  $x_1$ ,  $x_2$  and  $x_3$ .
- Perfect conductor condition at  $x_4$ .

The *layer 1* which is the space between the source of the wave and the sample) is assigned free space properties. The *layer 2* represents the sample and its conductivity and thickness are varied. *Layer 3* assigned for the properties of the free space and *layer 4* is an absorbing boundary condition.

The experimental results obtained for different test performed to demonstrate the wave behavior of the field inside the sample can be found at [7].

## Appendix C

# Relative Spatial Phase Patterns for Received and Transmitted $B_1$ Field

In this experiment [37], the study of the RF penetration in human body is performed with an eight-channel transceiver coil array that allows the use of an identical coil structure as a volume transmitted coil, multichannel receive coil or multiple single transmit surface coils. The tests are performed over a phantom.

Without studying to much in depth, for the receive  $B_1$  field, the complex image obtained after  $2D$  Fourier Transform the phase of the raw data from one channel at image coordinate  $r$  can be written as:

$$\Phi_{i,j}^{raw} = \varphi_{r,B_{1,j}^*rel} + \varphi_{0,j} + \varphi_{r,B_1com} + \varphi_{r,\Delta B_0} + \varphi_{r,res}, \quad (C.1)$$

For the  $\varphi_{r,B_1com}$  term we get:

$$\varphi_{r,B_1com} = \varphi_{r,B_1^+} + \varphi_{r,B_1^{-*}com}. \quad (C.2)$$

where  $j$  is the channel (or coil element). We can group the terms depending on whereas they depend or not with the coil topology and situation.

- Coil-specific terms.
  - $\varphi_{r,B_{1,j}^*rel}$  Is the coil-specific relative spatial phase. This term varies with coil and spatial position and is the one we want to estimate.
  - $\varphi_{0,j}$  Stands for the coil specific zero-order phase and it corresponds to a global phase shift for each channel. It depends on the relative polar position of the element in the circle formed by the eight coil elements, as well as on other hardware components inducing phase shifts. It can be estimated from the average phase of small ROI<sup>1</sup> at the center of the sample because coils are expected to have the same phase in that location.
- Coil-independent terms. Those terms account for  $B_0$  inhomogeneities:
  - $\varphi_{r,B_1com}$  is the coil common  $B_1$  phase.
  - $\varphi_{r,\Delta B_0}$  is the  $\Delta B_0$  phase derived from the phase of the complex ratio between two images acquired at  $10ms$  and  $6ms$  echo time ( $TE$ ).

---

<sup>1</sup>ROI stands for Region of Interest

–  $\varphi_{r,res}$  accounts here for a slight offset of  $k$ -space center.

Some of those terms had been estimated. Thus, the coil specific zero-order terms is:

$$\varphi_{0,j} \hat{=} \arg \left[ \sum \frac{\widehat{\mathbf{p}}_j^{raw} \exp(-j\gamma T_E \Delta B_0) \exp(-j)\varphi_{r,res}}{|\widehat{\mathbf{p}}_j^{raw}|} \right], \quad (\text{C.3})$$

where  $|\widehat{\mathbf{p}}_j^{raw}|$  is the pixel-wise form each channel value and  $\arg(|\widehat{\mathbf{p}}_j^{raw}|)$  its phase. Finally, the common phase term is estimate under the hypothesis that given the spherical symmetry of the phantom and the eightfold cylindrical symmetry of the coil structure

$$\varphi_{r,com} = \arg \left( \sum_j^N \frac{\widehat{\mathbf{p}}_{j,r}}{|\widehat{\mathbf{p}}_{j,r}|} \right), \quad (\text{C.4})$$

being N the number of coils. The pixelwise raw complex values are defined as:

$$\widehat{\mathbf{p}}_j = \widehat{\mathbf{p}}_j^{raw} \exp(-j\varphi_{0,j}) \exp(-j\gamma T_E \Delta B_0) \exp(-j\varphi_{r,res}). \quad (\text{C.5})$$

In the case of the transmitted  $B_1$  field we get a similar equation as for the one determined for the receive field but with some additional terms. The phase in complex data collected with coil element  $j$  when transmitting RF through coil element  $k$  is:

$$\Phi_{i,j,k}^{raw} = \varphi_{r,B_{1,j}^- rel} + \varphi_{r,B_{1,k}^+ rel} + \varphi_{0,j,k} + \varphi_{r,B_1 com} + \varphi_{r,\Delta B_0} + \varphi_{r,res}. \quad (\text{C.6})$$

and

$$\varphi_{r,B_1 com} = \varphi_{r,B_1 com}^+ + \varphi_{r,B_1 com}^{-*}. \quad (\text{C.7})$$

Removing the terms  $\varphi_{0,j,k}$ ,  $\varphi_{r,\Delta B_0}$  and  $\varphi_{r,res}$  from the raw data, we get and easier expression, which is the apparent phase expression:

$$\Phi_{i,j,k}^{app} = \varphi_{r,B_{1,j}^- rel} + \varphi_{r,B_{1,k}^+ rel} + \varphi_{r,B_1 com}. \quad (\text{C.8})$$

The estimation of the phase expression  $\varphi_{r,B_{1,k}^+ rel} + \varphi_{r,B_1 com}$  is obtained following:

$$\varphi_{r,B_{1,k}^+ rel} + \varphi_{r,B_1 com} = \varphi_{r,com} = \arg \left( \sum_j^N \frac{\widehat{\mathbf{p}}_{j,r,k}}{|\widehat{\mathbf{p}}_{j,r,k}|} \right). \quad (\text{C.9})$$

Those eight sums are put together in order to estimate  $\varphi_{r,B_1 com}$  as:

$$\varphi_{r,B_1 com} = \arg \left( \sum_{k=1}^N \sum_{j=1}^N \frac{\widehat{\mathbf{p}}_{j,r,k}}{|\widehat{\mathbf{p}}_{j,r,k}|} \right). \quad (\text{C.10})$$

Finally, each relative coil transmit phase  $\varphi_{r,B_{1,k}^+ rel}$  is derived from the previous equations getting:

$$\varphi_{r,B_{1,k}^+ rel} = \arg \left( \left( \sum_j^N \frac{\widehat{\mathbf{p}}_{j,r,k}}{|\widehat{\mathbf{p}}_{j,r,k}|} \right) \cdot \left( \sum_{k=1}^N \sum_{j=1}^N \frac{\widehat{\mathbf{p}}_{j,r,k}}{|\widehat{\mathbf{p}}_{j,r,k}|} \right)^* \right). \quad (\text{C.11})$$

## Appendix D

# Legendre Polynomials

Legendre functions are solutions to Legendre's differential equation:

$$\frac{d}{dx} \left[ (1-x^2) \frac{d}{dx} P_n(x) \right] + n(n+1)P_n(x) = 0. \quad (\text{D.1})$$

These solutions for  $n = 0, 1, 2, \dots$  (with the normalization  $P_n(1)=1$ ) form a polynomial sequence of orthogonal polynomials called the Legendre polynomials. Each Legendre polynomial  $P_n(x)$  is an  $n$ th-degree polynomial. It may be expressed using Rodrigues' formula:

$$P_n(x) = \frac{1}{2^n n!} \frac{d^n}{dx^n} [(x^2 - 1)^n]. \quad (\text{D.2})$$

Legendre Polynomials are used to estimate the bias in PABIC (see. Section 5.1) as they are smooth. This fact is needed because, as Styner assess in [?], the choice of an orthogonal basis result a better posed condition for changing the parameters  $p_i$ . Actually, the Legendre Polynomials are just one choice in between the other possibilities.

An important property of the Legendre polynomials is that they are orthogonal with respect to the L2 inner product on the interval  $-1 < x < 1$

$$\int_{-1}^1 P_m(x) P_n(x) dx = \frac{2}{2n+1} \delta_{mn}, \quad (\text{D.3})$$

(where  $\delta_{mn}$  denotes the Kronecker delta, equal to 1 if  $m = n$  and to 0 otherwise). In fact, an alternative derivation of the Legendre polynomials is by carrying out the Gram-Schmidt process on the polynomials  $1, x, x^2, \dots$  with respect to this inner product. The reason for this orthogonality property is that the Legendre differential equation can be viewed as a SturmLiouville problem

$$\frac{d}{dx} \left[ (1-x^2) \frac{d}{dx} P(x) \right] = -\lambda P(x), \quad (\text{D.4})$$

where the eigenvalue  $\lambda$  corresponds to  $n(n+1)$ . Polynomial at each coordinate are multiplied to define basis functions as:

$$P_l(\underline{x}) = \prod_{j=0}^{n-1} P_{l_j}(x_j). \quad (\text{D.5})$$

## Appendix E

# Optimization with (1+1)-ES algorithm

styner et al., in [31] had developed and nonlinear estimation for bias parametrization. This algorithm, randomly iterates select a new position in the parameter space being controlled by a probability function centered at the current position. The algorithm is summarized in [31] as:

$$r_t \sim N(0, I). \quad (\text{E.1})$$

$$\underline{x}_{t+1} = \underline{x}_t + a_t \underline{x}_t, \quad (\text{E.2})$$

where

$$a_{t+1} = a_t \cdot c_{grow}, \text{ if } f(\underline{x}_{t+1}) < f(\underline{x}_{opt}) \quad (\text{E.3})$$

$$a_{t+1} = a_t \cdot c_{shrink}, \text{ otherwise} \quad (\text{E.4})$$

and

$$x_{opt} = x_{t+1}, \text{ if } f(\underline{x}_{t+1}) < f(\underline{x}_{opt}) \quad (\text{E.5})$$

$$x_{opt} = x_{opt}, \text{ otherwise.} \quad (\text{E.6})$$

The parameters  $c_{grow}$ ,  $c_{shrink}$ ,  $a_0$  and  $x_0$  are given as a input and  $r_t \sim N(0, I)$  is a multidimensional random vector of an isotropic normal distribution with zero mean and variance one.

# List of Figures

1.1	Siemens MAGNET for 7 Tesla acquisitions . . . . .	3
2.1	Longitudinal magnetization and transverse magnetization values for a T1-weighted (a), and T2-weighted (b) images . . . . .	7
2.2	Types of MRI acquisition . . . . .	11
2.3	Transverse, sagittal and coronal view of a FLASH acquisition at 7T of a human brain . . . . .	13
2.4	Transverse, sagittal and coronal view of a MPRAGE acquisition of a human brain . . . . .	14
3.1	MPRAGE acquisition of a human brain corrupted by bias . . . . .	18
3.2	Histogram of brain tissue with IIIH. Figure (a) shows two different histograms obtained from BrainWeb-simulated database page ( <a href="http://www.bic.mni.mcgill.ca/brainweb">www.bic.mni.mcgill.ca/brainweb</a> ) one with noise and without IIIH (solid line) and the other with noise and IIIH (dashed line). Figure (b) is the histogram from a real brain image. . . . .	22
3.3	Hyper-intense region in the center of the head at 7T and its 3D view . . . . .	27
3.4	Grayscale plots of the transmission field and its circularly polarized components (a), and the contour plot of $\beta_t$ (b) of the quadrature surface coil in free space ( $\sigma = 0$ , $\epsilon_r = 1$ ). This plot is a ratio of the transmission field defined as $\beta_t \equiv \frac{ B_t^+ }{ B_t^+  +  B_t^- }$ . Image obtained from paper [16] . . . . .	28
5.1	2D human brain image used for first test in bias correction with PABIC. Single slice for a 7T MPRAGE acquisition corrupted by noise and bias (a) and plot of the computed histogram of its axial view (b). . . . .	40
5.2	2D human brain image used for first test in bias correction with PABIC. Single slice for a 7T MPRAGE acquisition corrupted by noise and bias (a) and the mask used for avoiding background (b). . . . .	41
5.3	Evolution of the elapsed time in simulation while changing pre-filter variance . . . . .	41
5.4	2D human brain image corrected with PABIC (a) and its grayscale profiles. Horizontal profile (b) and vertical profile (c). . . . .	42
5.5	Evolution of the p-vectors while increasing the number of maximum iterations allowed. . . . .	42
5.6	2D human brain image corrected with PABIC (a) and the evolution of the p-vectors while increasing the number of iterations up to 40000 (b). . . . .	43
5.7	Slice of a 3D volume human brain image corrected with PABIC (a) and its intensity histogram (b). . . . .	44

5.8	Vertical (a) and horizontal (b) profiles of gray values of one slice of a 3D human brain acquisition at 7T after PABIC correction with third degree of Legendre polynomials. . . . .	45
5.9	Central slices of the PABIC correction of a 3D human brain acquisition over 7T (from top to bottom, first row slices 90 to 93, second row slices from 94 to 97 and last row, slices from 98 to 101). . . . .	46
5.10	7T MPRAGE acquisition of human brain masked by direct threshold (a) and same acquisition skull stripped and de-noised (b) . (Both in sagittal view). . . . .	48
5.11	Block diagram of the LPF method proposed . . . . .	48
5.12	Ground truth for correction goodness' quantitative comparison. One single slice of a 3D volume in its axial view. Ground truth obtained by diving MPRAGE acquisition by parallel FLASH acquisition . . .	49
5.13	Evolution of the MSE between ground truth and image corrected by low pass filtering method when changing the variance and the window size of the filter (a) and evolution of the time elapsed in simulations (b). The low pass filter applied is the Gaussian filter. (variance values from 1 to 25 and window sizes from 1 to 80). . . . .	50
5.14	3 × 3 median filter operation. In (a) some samples of input pixel and its neighboring are displayed. The bright value of the output pixel is computed as shown in (b). . . . .	51
6.1	Single slice representation of the computed B1 magnitude map (a) and computed flip angle map (b) from an human brain at 7T. . . . .	56
6.2	Block diagram of the method proposed. Bias Correction by RF mapping . . . . .	58
6.3	Axial (transverse), sagittal and coronal view of a single slice of a 3D volume MPRAGE acquisition of 216x256x160 pixels before the correction using the RF mapping. . . . .	59
6.4	Axial (transverse), sagittal and coronal view of a single slice of a 3D volume MPRAGE acquisition of 216x256x160 pixels after the correction using the RF mapping. . . . .	59
B.1	Multiple propagation path in rectangular sample with large reflection coefficients at boundaries. . . . .	64
B.2	Sample with four different layers and their physical and electrical properties. . . . .	65

# Bibliography

- [1] Abduljalil AM, et al., *Enhanced gray and white matter contrast of phase susceptibility-weighted images in ultra high field magnetic resonance imaging*. Journal of Magnetic Resonance Imaging, vol.18, pp:284-290 (2003).
- [2] Akoka S. et al., *Radiofrequency map of an NMR coil by Imaging*. Medical Resonance in Medicine, vol.11, pp:437-441. (1993).
- [3] Axel, L., Constantini, et al., *Intensity Correction in surface coil MR imaging*. Am. J. Roentgenol, vol. 148, pp: 418-420 (1987).
- [4] Bach Cuadra, Meritxell *Atlas-based segmentation and classification of magnetic resonance brain images*. Thse EPFL, no 2875 (2003). Dir.: Jean-Philippe Thiran.
- [5] Belaroussi B, et al., *Intensity non-uniformity correction in MRI: Existing methods and their validation*. Medical Image Analysis, vol.10, pp: 234-246 (2006).
- [6] Ayres, Fan. *A Variational Approach to MRI Bias Correction*.
- [7] Caserta Jim, et al. *Reduction of wave phenomena in high field MRI experiments using absorbing layers*. Journal of Magnetic Resonance, vol. 169, pp.187-195 (2004).
- [8] Clare S., et al., *Compensating of  $B_1$  inhomogeneity using active transmit power modulation*. Magnetic Resonance Imaging, vol.19, pp:1349-1352 (2001).
- [9] Christoforidis GA, et al., *High resolution MRI of the deep brain vascular anatomy at 8 Tesla: susceptibility-based enhancement of venous structures*. J. Compt. Assist. Tomogr. vol 23, pp:857-66 (1999).
- [10] R.Deichmann et al., *Optimization of 3D MP-RAGE sequences for structural brain imaging*. NeuroImage. Vol.12, pp:112-127(2000).
- [11] R.Deichmann et al., *RF inhomogeneity compensation in structural brain imaging* Magnetic Resonance in Medicine, vol.47: pp.398-402 (2002)
- [12] *FSL Software Library* Analysis Group, FMRIB, Oxford, UK. <http://www.fmrib.ox.ac.uk/fsl/fsl>
- [13] Hashemi Ray, et al., *The Basics 2ED, 2004*.
- [14] Hiroaki M, et al., *Imaging of the dielectric resonance effects in high field magnetic resonance imaging*. Journal of applied physics, vol.97. 10R305 (2005).
- [15] *National Library of Medicine Insight Segmentation and Registration Toolkit*. <http://itk.org>

- [16] Jinghua, Wang et al., *Polarization of the RF field in human head at high field: a study with quadrature surface coil at 7.0 T* Magnetic Resonance in Medicine, vol.48, pp.362-369 (2002).
- [17] Jinghua, Wang et al., *Factors Influencing Flip Angle Mapping in MRI: RF Pulse Shape, Slice-Select Gradients, Off-Resonance Excitation and  $B_0$  Inhomogeneities*. Magnetic Resonance in Medicine, vol.56, pp.463-468 (2006).
- [18] Jiru, F. et al., *Fast 3D Radiofrequency Field Mapping Using Echo-Planar Imaging*. Magnetic Resonance in Medicine, vol.56, pp.1375-1379 (2006).
- [19] Lauterbur, et al., *Image formation by induced local interactions: examples of employing nuclear magnetic resonance*. Nature, vol 242, pp:190-191 (1973).
- [20] Lei H, et al. *in vivo P-31 magnetic resonance spectroscopy of the human brain at 7 Tesla: an initial experience*. Magnetic Resonance in Medicine, vol.49, pp. 199-205 (2003).
- [21] Lin, F-H., et al. *A wavelet-based approximation of surface coil sensitivity profiles for correction of image inhomogeneity and parallel imaging reconstruction*. Human Brain Mapping, vol.19, pp: 96-11 (2003).
- [22] Liney G., et al., *A simple method for the correction of endorectal surface coil inhomogeneity in prostate imaging*. Journal of Magnetic Resonance Imaging, vol.8 ,pp:994-997 (1998).
- [23] McRobbie D., et al., *MRI, From picture to proton, 2003*
- [24] S.Prima et al., *maximum likelihood estimation for the bias field in MR images: Investigating different modelings for the imaging process*. Proc.Med.Image Comp.Computer-Assist. Intervention - MICCAI 2001: 4th Conf.,Utrecht, The Netherlands, vol.2208, pp.811-819 (2001).
- [25] Qing X.yang et al., *Analysis of wave behaviour in lossy dielectric samples at high field*. Magnetic resonance in Medicine, vol 47: pp.982-989 (2002). DOI: 10.1002/mrm.10137.
- [26] S.Rice. *Mathematical Analysis of Random Noise*. Bell Sys. Tech. J., vol. 23, pp:282-332, July 1944.
- [27] Jan Grimm, et al., *MR imaging at 7T*. Center for Molecular Imaging Research.Department of Radiology, Massachusetts General Hospital. Medical Solution, January 2000.
- [28] J.Sijbers et al., *Maximum-likelihood estimation of Rician distribution parameters*. IEEE Transactions in Medical Imaging, vol. 17, No. 3,pp.357-361, June, 1998.
- [29] J.G. Sled et al., *A nonparametric method for automatic correction of intensity nonuniformity in MRI data*. IEEE Transactions in Medical Imaging, vol.17, No 1, pp.87-97,February 1998.
- [30] Stanislav Skora,, *K-space formulation of MRI*. <http://www.ebyte.it/library/educards/mri/K-SpaceMRI.html> March, 2005.
- [31] Martin Styner, et al., *Parametric Estimate of Intensity Inhomogeneities Applied to MRI*. March, 2000.
- [32] tang, L. et al., *On the Radio-frequency Power Requirements of Human MRI*. PIERS on Line, vol.3, No.6, (2007)

- [33] Thomas B, et al., *Approximate Boundary Conditions in Electromagnetics*. Bjrn Engquist and Gregory A. Kriegsmann, Eds. (1997)
- [34] Trong-Kha et al., *Effects of static radiofrequency magnetic field inhomogeneity in Ultra-High magnetic field resonance imaging*. Magnetic Resonance Imaging, vol. 24, pp:103-112(2006).
- [35] Ugurbil, Kamil. *Brain Imaging at 3T and Challenges at 7T* University of Minnesota medical School, Dept. of Radiology, Centre of Magnetic Resonance Research. Minneapolis, MN, USA.
- [36] Uros Vovk, et al., *A Review of Methods for Correction of Intensity Inhomogeneity in MRI*. IEEE Transactions in Medical Imaging, Vol 26, No.3. March 2007.
- [37] Van de Moortele, Pierre Francois et al., *B<sub>1</sub> destructive Interferences and Spatial Phase Patterns at 7T with a Head Transceiver Array Coil*. Magnetic Resonance in medicine. Vol 54, pp.1503-1518 (2005).
- [38] Vaughan T, et al., *How to do Rf at high fields* University of Minnesota Centre of Magnetic Resonance Research. Minneapolis, MN, USA. ISMRM, May 6-12, 2006.
- [39] Vokurka E., et al. *A Fast Model Independent Method for Automatic Correction of Intensity Non-uniformity in MRI data*. Journal of Magnetic Resonance Imaging, vol.10, pp: 550-562 (1999).
- [40] Peña Piña, Xavier. *Bias Field Correction in Magnetic Resonance Images of a Rat Brain*. ITS, Swiss Federal Institute of Technology (EPFL). September 2007.
- [41] Zujun, Hou. *A Review on MR Image Intensity Inhomogeneity Correction*. Hindawi Publishing Corporation. International Journal of Biomedical Imaging, vol. 2006, pp:1-11. ID 49515, DOI:10.1155/IJBI/2006/49515
- [42] <http://www.tesisenxarxa.net/TESISUB/AVAILABLE/TDX-0311105-110752//1.INTRODUCCION.pdf>;2008